Accounting for plasticity: An extension of inelastic Constitutive Artificial Neural Networks

Birte Boes^a, Jaan-Willem Simon^a, Hagen Holthusen^b

^a Computational Applied Mechanics, University of Wuppertal, Pauluskirchstrasse 7, 42285 Wuppertal, Germany
^b Institute of Applied Mechanics, RWTH Aachen University, Mies-van-der-Rohe-Str. 1, 52074 Aachen, Germany

Abstract

The class of Constitutive Artificial Neural Networks (CANNs) represents a new approach of neural networks in the field of constitutive modeling. Through consideration of constitutive constraints such as objectivity, material symmetry, thermodynamical consistency, and polyconvexity, the results predicted by the neural networks are physically reasonable as they a priori fulfill the principle of thermodynamics. This leads to physically sound material models that are capable of predicting suitable material behavior even outside the trained data range. So far, CANNs have proven to be a powerful tool in predicting elastic and inelastic material behavior. However, the specification of inelastic constitutive artificial neural networks (iCANNs) to capture plasticity remains to be discussed.

We present the extension and application of an iCANN to the inelastic phenomena of plasticity. This includes the prediction of a formulation for the elastic and plastic Helmholtz free energies, the inelastic flow rule, and the yield condition that defines the onset of plasticity. Thus, we learn four feed-forward networks in combination with a recurrent neural network and use the second Piola-Kirchhoff stress measure for training. The presented formulation captures both, associative and non-associative plasticity. In addition, the formulation includes kinematic hardening effects by introducing the plastic Helmholtz free energy. This opens the range of application to a wider class of materials.

The capabilities of the presented framework are demonstrated by training on artificially generated data of models for perfect plasticity of von-Mises type, tension-compression asymmetry, and kinematic hardening. We observe already satisfactory results for training on one load case only while extremely precise agreement is found for an increase in load cases. In addition, the performance of the specified iCANN was validated using experimental data of X10CrMoVNb9-1 steel. Training has been performed on both, uniaxial tension and cyclic loading, separately and the predicted results are then validated on the opposing set. The results underline that the autonomously discovered material model is capable to describe and predict the underlying experimental data.

Keywords: Constitutive artificial neural networks, Automated model discovery, Machine learning, Plasticity, Kinematic hardening, Constitutive modeling



Nomenclature	
a	Scalar quantity
$\mid a \mid$	First order tensor
$oldsymbol{A}$	Second order tensor
(*)	Total derivative with respect to time
$(*)^T$	Transpose of a quantity
$(*)^{-1}$	Inverse of a quantity
abs(*)	Absolute value of a quantity
$\cosh(*)$	Cosinus hyperbolicus of a quantity
$\det(*)$	Determinant of a quantity
dev(*)	Deviatoric part of a quantity
$\exp(*)$	Exponential of a quantity
$\ln(*)$	Logarithm of a quantity
$\operatorname{sym}(*)$	Symmetric term of a quantity
$\mathrm{tr}(*)$	Trace of a quantity
$(\overset{-}{*})$	Quantity defined in the co-rotated intermediate configuration
A:B	Scalar product of two tensors \boldsymbol{A} and \boldsymbol{B}
$I_1^{m A}$	$\mathrm{tr}(oldsymbol{A})$
$I_2^{m A}$	$1/2 \left[\operatorname{tr}(\boldsymbol{A})^2 - \operatorname{tr}(\boldsymbol{A}^2) \right]$
$I_3^{m A}$	$\det({m A})$
$J_2^{m A}$	$1/2\operatorname{tr}(\operatorname{dev}(\boldsymbol{A})^2)$
$J_3^{m A}$	$1/3\operatorname{tr}(\operatorname{dev}(\boldsymbol{A})^3)$

1. Introduction

Plasticity

Natural and synthetically manufactured materials classically undergo irreversible effects under loading. While we relate reversible deformation mechanisms to elastic material behavior, the irreversible or inelastic deformations often can be assigned to plastic deformations that occur after yielding of the materials. The effects causing plasticity can differ considering the underlying material. While, for example, crystal dislocations lead to plastic behavior in metals (c.f. Kuhlmann-Wilsdorf (1999); Aoyagi et al. (2014)), the relative movement of the grains is responsible in soil mechanics (Terzaghi et al., 1996; Borja, 2013). The different effects on the microscale cause a variety of macromechanical phenomena. One of which is tension-compression asymmetry that comes into account for thermoplastic polymers, often used due to their high flexibility and

cost-efficiency (Felder et al., 2020; Reuvers et al., 2024), carbon-reinforced plastics (Stier et al., 2015), and more. This asymmetry also comes into account in the emerging field of additive manufacturing as shown by Motaman and Haase (2021) or Ghorbanpour et al. (2021). However, not only the onset of yielding but also the inelastic evolution afterwards requires special observation. Thus, hardening effects such as isotropic and kinematic hardening are required to account for the Bauschinger effect, for example (Chun et al., 2002; Gau and Kinzel, 2001).

To gain knowledge of the behavior, a tremendous amount of material models has been established throughout the years aiming to predict the material response adequately. While the fundamental works of Hencky (1924); von Mises (1913); Coulomb (1776) have been applied and improved in numerous applications, the technical improvement impose ever new emerging materials and failure mechanisms. One of the main issues is to maximize the loading capacities of structures consisting out of these new materials. This requires appropriate material models to accurately predict the underlying material behavior and failure mechanisms.

Neural networks

Regarding the field of computational mechanics, these new materials require novel material models to accurately predict the material behavior. The technological improvements have not only led to new manufacturing processes, but also to an increase in computational performance. Thus, the field of machine learning has emerged widely. What logically follows, is a combination of the constitutive modelling and machine learning approaches to simplify the time-consuming elaboration of adequate material models. The major point of interest is the relation between strains and stresses. Thus, we seek to describe a function that relates any strain data to the resulting stresses or vice versa. This mechanical relation has lately been resolved by incorporating neural networks which are of high interest. Hence, a tremendous amount of approaches to capture material behavior has been published throughout the last years. One of them are artificial neural networks (ANNs), that can handle complex nonlinear data sets (Drew and Monson, 2000). Stress and strain data have been related to each other by black-box regression approaches (Ghaboussi et al., 1991). While improvement of the computational parts has led to promising results, the mechanical constraints have been violated as the principles of materials theory and thermodynamics are not automatically fulfilled. This leads to a wide range of training data required and, in addition, the extrapolation of the models beyond the training regime is insufficient. Inclusion of thermodynamic constraints has been incorporated though a correction in the post-processing step (see Kalina et al. (2022, 2023b)) or by adding physical terms to the loss function as in physically informed neural networks (PINNs) (Karniadakis et al., 2021; Raissi et al., 2019). Classically, PINNs are applied to solve ordinary differential equations (Linka et al., 2022) or partial differential equations (Raissi et al., 2019) but are also applied to constitutive modeling, for example by Haghighat et al. (2023) or Tac et al. (2023) based on neural ordinary differential equations (NODEs).

However, these approaches lack the interpretation of the predicted models found by the neural networks and might not always fulfill the laws of continuum mechanics. However, we aim to learn from the given stress strain relation and find the constitutive relations that predict the underlying material behavior. The constitutive equations are taken into account by defining strain invariants as inputs and energy functions as outputs by Shen et al. (2004) and Zopf and Kaliske (2017) who have met experimental data of rubber-like materials (Blatz and Ko, 1962). Incorporation of principles of thermodynamics remains an important aspect as shown by Masi et al. (2021). They present a thermodynamics based neural network that addresses the first and second law of thermodynamics and special activation functions which results in a faster training and requires a smaller amount of data for training. Application to rubber-like materials and capturing rate-independent inelasticity using two feed-forward neural networks (FFN) for the inelastic evolution and the free energy has been discussed by Ghaderi et al. (2020), Masi et al. (2021) and Masi and Stefanou (2022). Automated model discovery to link stresses and strains has been applied by Martonová et al. (2024) and Peng et al. (2021) and on human brain cortex by Hou et al. (2024) and have been embedded into finite element analysis software (Peirlinck et al., 2024).

Next to the general approach of relating stress-strain data, the application to inelasticity has been discussed throughout widely. While a training with internal state variables has been applied by Masi et al. (2021) and Masi and Stefanou (2022), the internal state variables are passed through the hidden states of the recurrent neural network (RNN) in the work of He and Chen (2022). However, nonzero dissipation is not automatically ensured for arbitrary load cases. In contrast, thermodynamic consistency is fulfilled by the design of the network architecture presented in Amos et al. (2017) who present a combination of the concept of generalized standard materials (Miehe, 2002) with input convex neural networks (ICNN) and the application to visco-elasticity. Based on the concept of generalized standard materials, physics-augmented neural networks capturing inelasticity have been applied by Rosenkranz et al. (2023a), Rosenkranz et al. (2023b) and Linden et al. (2023). Considering elasto-plasticity, replacing parts of the constitutive models such as the yield criterion by neural networks has been shown by Settgast et al. (2020); Malik et al. (2021); Vlassis and Sun (2021b,a); Fuhg et al. (2023). Meyer and Ekre (2023) or using a constrained neural network for elasto-plasticity (Weber et al., 2023).

As pointed out above, considering the principles of material theory and thermodynamics is a major point in constitutive modeling and has already been incorporated into several modelling approaches. These constraints directly reduce the amount of data required for training. Using neural networks, we not only aim to find a relation between stresses and strains but rather predict the material model itself. Such physically reasonable models enable the prediction even outside the training regime which is a clear advantage. Thus, a new machine learning architecture has been established that are constitutive artificial neural networks (CANNs) (Linka et al., 2021; Linka and Kuhl, 2023). They incorporate the principles of material symmetry, objectivity, etc. a priori by means of their general structure and fulfill thermodynamic consistency

a priori instead of adding penalty terms to the loss function as done by Weber et al. (2023) or Kalina et al. (2023a). By means of their architecture, physically reasonable formulations of the Helmholtz free energy functions are designed in terms of strain invariants as inputs. This general formulation has recently been applied to tremendous applications such as alzheimer disease Zhang et al. (2024); Stockman et al. (2024), brain cortex Hou et al. (2024), cardiac tissue Martonová et al. (2024), mechanics of artificial meat Pierre et al. (2023) and many more. In addition, the extension to inelasticity has already been shown by Abdolazizi et al. (2023) and Holthusen et al. (2023a). So far, the specification of iCANNs to plasticity remains to be discussed. However, the prediction of irreversible effects such as plasticity is of great interest as it dominates in various materials.

Outline

This work aims to expand the class of CANNs to capture elasto-plastic material behavior in a general manner while fulfilling the principles of material theory and thermodynamics. It is based on the general framework of iCANNs and expands their application to restricted solution domains. In this work, we restrict the discussion to plasticity and therefore introduce the label of iCANNp. Considering finite strains, stress definitions are derived from elastic and plastic Helmholtz free energy definitions resulting from the second law of thermodynamics. To fulfill thermodynamic consistency, the inelastic evolutions are derived from plastic potentials. The underlying fundamentals of materials theory and the principles of thermodynamics are described in Section 2. Section 3 describes the design of the feed-forward networks of the elastic and plastic Helmholtz free energies and plastic potentials. All of them are revised in Section 4, where a specification of each network structure is discussed for the numerical investigation following in Section 5. We validate the performance of the described iCANNp by artificially generated data of perfect plasticity with von Mises-type and asymmetric yield criteria, and investigate the prediction of kinematic hardening. In addition, predictions of uniaxial tension and cyclic loading of experimental data of X10CrMoVNb9-1 steel are discussed. Section 6 completes with a conclusion of the presented iCANNp.

2. Constitutive Modeling

In the following, the constitutive framework, which is the basis for the constitutive artificial neural network, is presented. The characteristic equations are derived following the principles of thermodynamics such that a thermodynamically consistent formulation is found. Including plastic effects, we end up with a general formulation of elastic and plastic quantities.

2.1. Kinematics

We consider finite strains and use the multiplicative decomposition of the total deformation gradient $\mathbf{F} = \mathbf{F}_e \mathbf{F}_p$ into an elastic and plastic component \mathbf{F}_e and \mathbf{F}_p , respectively (see Lee and Liu (1967); Lee

(1969)). Considering superposed rigid body motions, the deformation gradient reads $F^+ = QF$ for all proper orthogonal tensors $Q \in SO(3)$. In addition, we can apply rigid body motions of the reference configuration, $F^* = FQ^T$. The assumption of material symmetry and objectivity then leads us to the introduction of the right Cauchy-Green deformation tensor, $C = F^T F$, which remains unchanged under spatially superposed rigid body motions (Ogden, 1997; Holzapfel, 2002; Simo and Hughes, 2006). The decomposition of the deformation gradient results in an elastic and plastic part of the total right Cauchy-Green deformation tensor, $C_e = F_e^T F_e$ and $C_p = F_p^T F_p$. Similar arguments hold true for the left Cauchy-Green tensor, $B = FF^T$

Co-rotated intermediate configuration The multiplicative split is associated with a fictitious, unstressed intermediate configuration that suffers from a rotational non-uniqueness. Most material models that capture inelasticity are derived with respect to this intermediate configuration. However, since this configuration is not uniquely defined, neither are the quantities defined with respect to the intermediate configuration. Thus, neither stress- nor strain-like quantities in the intermediate configuration can be computed as they suffer from the rotational non-uniqueness and in general, pull-back operations are required. Considering the polar decomposition of the deformation gradient into stretch and rotation tensors by F = RU = VR, we can conclude that only the rotation tensor, R, is affected by this rotational non-uniqueness. Following the concept presented by Holthusen et al. (2023b), a co-rotated intermediate configuration is introduced as a co-rotated pull-back from the intermediate configuration, $(\bar{\bullet}) = R_p^{-1}(\bar{\bullet})R_p^{-1}$. Consequently, we can introduce for example the co-rotated elastic right and left Cauchy-Green tensors

$$\bar{C}_e = U_p^{-1} C U_p^{-1} \tag{1}$$

$$\bar{B}_{v} \equiv C_{v}.$$
 (2)

In consequence, all quantities with respect to the co-rotated intermediate configuration are uniquely defined and can be computed directly. The eigenvalues and symmetry properties between the intermediate configuration and the co-rotated one remain the same, and the assumption of an unstressed intermediate configuration holds true for the co-rotated one. For more information on the concept of the co-rotated intermediate configuration, the reader is referred to the works of Holthusen et al. (2023b), Boes et al. (2023) and the literature cited therein.

To phenomenologically describe the material behavior, a Helmholtz free energy is introduced as an isotropic function of the elastic and inelastic quantities and thus $\psi = \hat{\psi}(C_e, B_p)$. Following the arguments above and Equations (1) and (2), we can similarly write

$$\psi_0 = \hat{\psi}(\bar{C}_e, C_p). \tag{3}$$

Isochoric-volumetric decomposition We further use the multiplicative split into isochoric and volumetric

components originally introduced by Flory (1961) and applied to finite strains by Lubliner (1985), Simo and Taylor (1991) and Simo et al. (1985). Thus, we have

$$\mathbf{F} = J_F^{1/3} \tilde{\mathbf{F}}, \quad \mathbf{C} = J^{1/3} \tilde{\mathbf{C}} \tag{4}$$

where $J_{\boldsymbol{F}} = \det(\boldsymbol{F})$ and $J = \det(\boldsymbol{C})$. The modified deformation gradient and right Cauchy-Green tensor, $\tilde{\boldsymbol{F}} = J_{\boldsymbol{F}}^{-1/3} \boldsymbol{F}$ and $\tilde{\boldsymbol{C}} = J^{-1/3} \boldsymbol{C}$, are linked to volume-preserving deformations, and the terms with $J^{1/3}$ to volume-changing deformations.

In general, we can describe the deformation state of an isotropic material in terms of the principal invariants of the right Cauchy-Green deformation, which are $I_1^{\mathbf{C}} = \operatorname{tr}(\mathbf{C})$, $I_2^{\mathbf{C}} = 1/2 \left([\operatorname{tr}(\mathbf{C})]^2 - \operatorname{tr}(\mathbf{C}^2) \right)$ and $I_3^{\mathbf{C}} = \det(\mathbf{C})$. Introduction of Relation (4) leads to a new set of invariants of

$$\tilde{I}_1 = \operatorname{tr}(\tilde{C}) = \frac{I_1}{I_3^{1/3}}, \quad \tilde{I}_2 = \frac{1}{2} \left([\operatorname{tr}(\tilde{C})]^2 - \operatorname{tr}(\tilde{C}^2) \right) = \frac{I_2}{I_3^{2/3}}$$
 (5)

which we refer to as the isochoric formulations (Hartmann and Neff, 2003; Schröder and Neff, 2003).

2.2. Derivation based on Clausius-Planck inequality

To derive the constitutive equations, the Clausius-Planck inequality, $-\dot{\psi} + \mathbf{S} : 1/2\dot{\mathbf{C}} \geq 0$, is evaluated. Here, \mathbf{S} is the second Piola-Kirchhoff stress. As stated above, the Helmholtz free energy is defined in terms of elastic and plastic terms. Thus, taking its time derivative

$$\dot{\psi} = \frac{\partial \psi}{\partial \bar{C}_e} : \dot{\bar{C}}_e + \frac{\partial \psi}{\partial C_p} : \dot{C}_p. \tag{6}$$

with the rates $\dot{\bar{C}}_e = U_p^{-1}\dot{C}U_p^{-1} - \bar{C}_e\bar{L}_p - \bar{L}_p^T\bar{C}_e$ and $\dot{C}_p = \bar{L}_p^TC_p + C_p\bar{L}_p$, where $\bar{L}_p = \dot{U}_pU_p^{-1}$ holds, and following the arguments of Coleman and Noll (1961) leads to

$$\left(S - 2U_p^{-1} \frac{\partial \psi}{\partial \bar{C}_e} U_p^{-1}\right) : \frac{1}{2}\dot{C} + \underbrace{\left(2\bar{C}_e \frac{\partial \psi}{\partial \bar{C}_e} - 2\frac{\partial \psi}{\partial C_p} C_p\right)}_{=:\bar{\Sigma}} : \bar{L}_p \ge 0.$$
(7)

from which we define the state relations of the second Piola-Kirchhoff stress, S, the relative stress, $\bar{\Gamma} = \bar{\Sigma} - \bar{\chi}$, the Mandel stress, $\bar{\Sigma}$, and the backstress, $\bar{\chi}$. The latter one is related to kinematic hardening and describes the translation of the origin of the yield surface during plastic deformations. While neither the backstress nor the Mandel stress are generally symmetric, the relative stress is (cf. Svendsen (2001)). Hence, we can replace the rate of inelastic strains with its symmetric part, $\bar{D}_p := \text{sym}(\bar{L}_p)$ leading to the reduced inequality as

$$\mathcal{D}_{\text{red}} = \bar{\mathbf{\Gamma}} : \bar{\mathbf{D}}_{p} \ge 0 \tag{8}$$

which must be fulfilled for arbitrary thermodynamical processes. Therefore, evolution laws must be formulated that ensure the fulfillment of Inequality (8). For this, a potential as a scalar-valued isotropic function of the thermodynamic driving force $g = \hat{g}(\bar{\Gamma})$ is introduced, and the evolution law is assumed to be

$$\bar{D}_p = \dot{\lambda} \frac{\partial g}{\partial \bar{\Gamma}}, \quad \dot{C}_p = 2\dot{\lambda} U_p \frac{\partial g}{\partial \bar{\Gamma}} U_p.$$
 (9)

Considering inelastic effects of plasticity here only, $\dot{\lambda}$ can be interpreted as a plastic multiplier. Regarding a wider class of inelasticity, it can be interpreted, for example, as a relaxation time in visco-elasticity or a growth multiplier for growth modeling (c.f. Lamm et al. (2021); Lamm and Holthusen (2022)). The plastic multiplier is per definition non-negative and is defined through the Karush-Kuhn-Tucker conditions, i.e.

$$\dot{\lambda} \ge 0, \quad \Phi \le 0, \quad \dot{\lambda} \Phi = 0.$$
 (10)

They complete the set of constitutive equations and introduce the yield function, which encloses the elastic regime. For any stress state within the boundary of the yield surface, the plastic multiplier must be equal to zero, leading to no plastic strain evolution. Thus, the inequalities in Equation (10) describe the material behavior associated to the current stress state and must be fulfilled at all times. For the special case of associative plasticity, the plastic potential describing the evolution of plastic flow is equal to the yield function, i.e. $\bar{D}_p = \dot{\lambda} \partial \Phi / \partial \bar{\Gamma}$. Up to now, the constitutive equations have been derived in a general manner. It remains to find specific formulations for the Helmholtz free energy and the yield function or/and the plastic potential that will be discussed in more detail in the following.

2.3. Requirements on the Helmholtz free energy

For a constitutive model, we derive the stress response from a scalar-valued Helmholtz free energy function ψ as stated in Equation (7). The Helmholtz free energy is only affected by stretches and not by rotations. Together with this criterion, we formulate it in terms of the right Cauchy-Green tensor and conclude ψ to be an isotropic function of its arguments being invariant of C (Holzapfel (2002)). We can therefore describe it in terms of the principal invariants of its arguments, I_1^C , I_2^C , and I_3^C . For more information, the reader is referred to the fundamental works of Gurtin (1982) and Truesdell et al. (1992), for example.

Following the normalization condition, we imply the Helmholtz free energy function to be zero-valued at the origin, i.e. $\psi(\mathbf{I}) = 0$. In addition, it must fulfill a stress-free reference configuration (Holzapfel (2002)).

Physically, the energy must tend to infinity for an infinite compression or expansion of the continuum. Mathematically, it has to hold that ψ tends to $+\infty$ when I_3 tends to $+\infty$ or 0^+ , or when I_1 or I_2 approach $+\infty$ which is also called the growth criterion. Therefore, we separate the energy into isochoric and volumetric terms and decompose it into subfunctions to ensure polyconvexity. Fulfilling the normalization criterion and following the approaches in (Hartmann and Neff, 2003) and (Schröder and Neff, 2003), we end up with

$$\psi = \psi_1(\tilde{I}_1 - 3) + \psi_2(\tilde{I}_2^{3/2} - 3\sqrt{3}) + \psi_3(I_3 - 1)$$
(11)

that serves as the general basis for the elastic and plastic Helmholtz free energy functions. They will be further described in the design of the network structure in Section 3.

Describing not only elastic effects but also inelastic ones, we have multiplicatively decomposed the deformations and consequently define the Helmholtz free energy in terms of invariants of \bar{C}_e and C_p , i.e.

$$\psi_0 = \psi(\bar{C}_e, C_p) = \psi(I_1^{\bar{C}_e}, I_2^{\bar{C}_e}, I_3^{\bar{C}_e}, I_4^{\bar{C}_e, C_p}, I_5^{\bar{C}_e, C_p}, I_6^{\bar{C}_e, C_p}, I_7^{\bar{C}_e, C_p}, I_1^{C_p}, I_2^{C_p}, I_3^{C_p})$$
(12)

Here, the mixed invariants $I_4^{\bar{C}_e, C_p} = \operatorname{tr}(\bar{C}_e C_p)$, $I_5^{\bar{C}_e, C_p} = \operatorname{tr}(\bar{C}_e^2 C_p)$, $I_6^{\bar{C}_e, C_p} = \operatorname{tr}(\bar{C}_e C_p^2)$ and $I_7^{\bar{C}_e, C_p} = \operatorname{tr}(\bar{C}_e^2 C_p^2)$ are introduced. We restrict the elastic and plastic formulations to depend only on the elastic and plastic terms of the right Cauchy-Green tensors, respectively, and therefore exclude all mixed invariants. Moreover, we additively decompose the energy into an elastic and plastic part by

$$\psi = \psi_e(\bar{C}_e) + \psi_p(C_p). \tag{13}$$

as we consider isotropic materials here only. The latter part, ψ_p , is related to kinematic hardening. Both terms follow the structure given in Equation (11).

2.4. Requirements on the plastic potentials

Next to the Helmholtz free energy, a formulation for plastic material behavior must be found. In (Holthusen et al., 2023a), the class of CANNs has been extended to inelasticity by introducing a pseudo potential to formulate the evolution of inelastic quantities. This formulation is the foundation of the extension to plasticity presented here. We can separate the plastic formulation into the definition of the onset of plasticity and its evolution and describe both response functions in the stress space in terms of our relative stress, which includes the Mandel stress and internal variables, which are defined here as the backstress to account for kinematic hardening.

2.4.1. Yield surface

In a first step, we focus on the yield condition. Considering any point in the stress space, the elastic domain can be encircled by an initial yield surface Φ . This initial yield function encloses all elastic stress states and, thus, defines the elastic domain, $\operatorname{int}(\mathbb{E}) = \{\bar{\Gamma} \in \mathbb{R} \mid \Phi(\bar{\Gamma}) < 0\}$. The boundary of the elastic domain, $\partial \mathbb{E} = \{\bar{\Gamma} \in \mathbb{R} \mid \Phi(\bar{\Gamma}) = 0\}$, defines the plastic domain. All stress states outside the yield surface are not allowed such that all admissible stress states are within the set of \mathbb{E} . Conclusively, $\operatorname{int}(\mathbb{E})$ is be a closed interval which enforces Φ to be a convex function (Borja, 2013).

We can generally describe the yield function by a stress-dependent part that we introduce by a potential $\hat{h}(\bar{\Gamma})$ and a parameter c that can be related to the initial yield stress, i.e. $\hat{\Phi}(\bar{\Gamma}) = \hat{h}(\bar{\Gamma}) - c = 0$. We can further introduce the relation $h = 1/c \hat{h}$ and end with a general formulation of the yield function defined in terms of a potential $h(\bar{\Gamma})$, i.e.

$$\Phi(\bar{\Gamma}) = h(\bar{\Gamma}) - 1 = 0. \tag{14}$$

Thus, to define the boundary of the elastic regime, we need to find a formulation for h which is an isotropic function of its argument. In consequence, we can describe it in terms of its integrity basis, $h(\bar{\Gamma}) = h(I_1^{\bar{\Gamma}}, J_2^{\bar{\Gamma}}, J_3^{\bar{\Gamma}})$. The choice of invariants has been made according to sophisticated formulations of inelastic potentials (see Tschoegl (1971); Ghorbel (2008)). Physically, the first invariant, $I_1^{\bar{\Gamma}}$, can be interpreted as the hydrostatic pressure to account for pressure-dependency while the second deviatoric stress invariant, $J_2^{\bar{\Gamma}}$, captures the amount of shear stresses and the third, $J_3^{\bar{\Gamma}}$, the direction and state of stress. While the set of the stress invariants is a common choice, the inelastic potential might also be described in terms of principal stresses (c.f. Tresca (1869); Yu (2002)) or the Lode angle (c.f. Zienkiewicz (1977)).

Analogously to Equation (11), we express it in terms of a Taylor series by To ensure convexity, we express the potential in terms of subfunctions by

$$h(\bar{\Gamma}) := h_1(I_1^{\bar{\Gamma}}) + h_2(J_2^{\bar{\Gamma}}) + h_3(J_3^{\bar{\Gamma}}). \tag{15}$$

where each subfunction can be described by a convex activation function which will be described in more detail in the following chapter. In addition, we require the potential to be zero-valued an non-negative, which is automatically fulfilled by the terms including $J_2^{\bar{\Gamma}}$. To ensure non-negativity of the terms formulated by $I_1^{\bar{\Gamma}}$ and $J_3^{\bar{\Gamma}}$, we will use convex, non-negative activation functions that will be described in Section 3 in more detail.

The additive formulation of the potential might yield to non-smooth intersections which can lead to numerical problems. To avoid sharp corners in the design of the potential, a smoothing technique as described in (Gesto Beiroa et al., 2011) such as the p-norm regularization presented by Mollica and Srinivasa (2002) is applied. We adjust the definition of the potential accordingly

$$h(\bar{\mathbf{\Gamma}}) = \left(\sum_{i=1}^{n} \left| h_i(\bar{\mathbf{\Gamma}}) \right|^p \right)^{1/p} \tag{16}$$

where h_i are convex functions, p is a positive parameter and n is the number of subpotentials. With increasing p, the resulting boundary adapts to the initial surface whereas the intersections remain smooth. Visualization can be found in Figure 1 exemplarly for the two intersecting functions $f_1 = (\sigma_1 + \sigma_2)^2 - 1$ and $f_2 = (\sigma_1 - \sigma_2)^2 + (\sigma_2)^2 + (-\sigma_1)^2 - 1$ at the x-y-plane for p = 1, 2, 3. As we require our potential to be convex, non-negative and zero-valued at the origin, we automatically ensure a smooth surface since these functions fulfill the same criteria as the absolute function and thus, Equation (16) is fulfilled for p = 1.

2.4.2. Flow rule and hardening laws

Having defined the criteria for the onset of plastic behavior, the evolution of plastic strains must be described. For this, the flow rule in Equation (9) is given. It is described by the plastic multiplier $\dot{\lambda}$, which gives information about the magnitude of the plastic evolution, and by the derivative of a plastic potential with respect to its argument. Following the normality rule, the latter one describes the direction of the

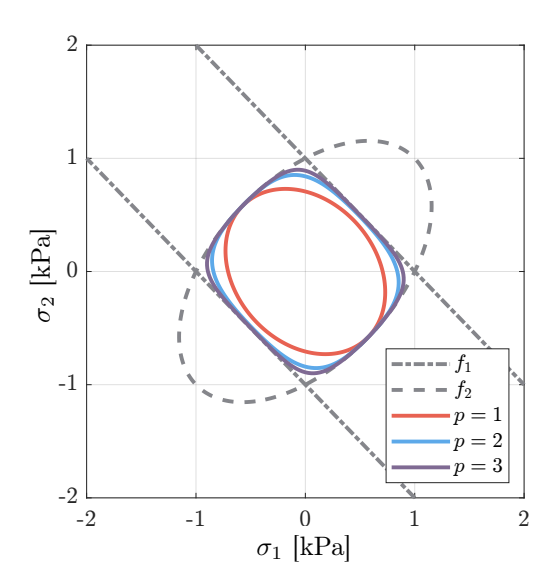


Figure 1: Schematic visualization of the p-norm regularization used for smooth intersection of the functions f_1 and f_2 (given in gray) for three different p-values (p = 1 in red, p = 2 in blue, p = 3 in purple).

plastic rate of deformation being defined as the normal to the plastic potential. From this, it is obvious, that a non-smooth potential leads to problems in the computation of the plastic flow as its derivative in a non-smooth intersection does not exist. The plastic potential can, in general, be defined similarly to the yield surface stated above, such that

$$g(\bar{\Gamma}) = g_1(I_1^{\bar{\Gamma}}) + g_2(J_2^{\bar{\Gamma}}) + g_3(J_3^{\bar{\Gamma}}). \tag{17}$$

For associative plasticity, the potential is equal to the one of the yield surface, i.e. $g \equiv h$. However, the following derivation will be held general such that both, the associative and non-associative case, are handled. From Equation (17), the flow rule can be defined by Equation (9).

2.4.3. Multisurface plasticity

As stated in Section 1, the definition of the elastic regime might not be sufficiently described by one yield surface only. Therefore, multisurface plasticity is used to more adequately describe, for example, the pre-failure behavior of soils and rock mechanics (Desai and Siriwardane, 1984; Chen, 2007), metals (Bedzra et al., 2017; Keralavarma, 2017) or paper and paperboard (Xia et al., 2002; Bedzra et al., 2019; Alzweighi et al., 2023). The elastic domain is then bounded by a set of n independent, convex surfaces which might intersect non-smoothly. We can express the elastic domain by the inner domain of all yield functions Φ_i , i.e. $\operatorname{int}(\mathbb{E}) = \{\bar{\Gamma} \in \mathbb{R} \mid \Phi_i(\bar{\Gamma}) < 0, i = 1, n\}$. The yield surface is then defined by the set of all stresses such that $\Phi_i(\bar{\Gamma}) = 0$ for at least one i and $\Phi_j(\bar{\Gamma}) \leq 0$ for all $j \neq i$ (see de Souza Neto et al. (2011)). While the convex domain has a smooth boundary, the intersection of the yield functions might not. This can be difficult from a computational point of view as the gradient of the plastic potential must be derived. The

elastic domain therefore can be approximated with a smooth domain as proposed by Adhikary et al. (2017). To ensure a general approach for the design of the neural network, we choose a linear combination of all subgradients $N_i = \partial g_i/\partial \bar{\Gamma}$ to define the evolution of plastic flow. With this, we define plastic loading and consistency conditions for each yield surface separately. In consequence, the set of conditions expands to n conditions of $\dot{\lambda}_i \geq 0$, $\Phi_i \leq 0$ and $\dot{\lambda}_i \Phi_i = 0$ (no summation of repeated indices). The mechanical answer becomes then multilinear (Houlsby and Puzrin, 2007). Each yield function Φ_i can be defined in the manner of Equation (15). Then, the flow rule is expressed in terms of multiple potentials g_i by

$$\bar{\mathbf{D}}_{p} = \sum_{i=1}^{n} \dot{\lambda}_{i} \frac{\partial g_{i}}{\partial \bar{\mathbf{\Gamma}}} \tag{18}$$

In the case of associative plasticity, the flow rule is then defined in terms of the gradients of the yield surfaces such that $\bar{D}_p = \sum_{i=1}^n \dot{\lambda}_i \, \partial \Phi_i / \partial \bar{\Gamma}$ holds.

2.4.4. Thermodynamical consistency

Having introduced the onset and evolution of plasticity, it remains to prove thermodynamical consistency of the model. We recall Inequality (8) and the flow rule in Equation (18) together with Equation (17), and obtain

$$\mathcal{D}_{\text{red}} = \sum_{i=1}^{n} \dot{\lambda}_{i} \left(\frac{\partial g_{1i}}{\partial I_{1}^{\bar{\Gamma}}} I_{1}^{\bar{\Gamma}} + 2 \frac{\partial g_{2i}}{\partial J_{2}^{\bar{\Gamma}}} J_{2}^{\bar{\Gamma}} + 3 \frac{\partial g_{3i}}{\partial J_{3}^{\bar{\Gamma}}} J_{3}^{\bar{\Gamma}} \right) \ge 0.$$
 (19)

The derivatives $(\partial I_1^{\bar{\Gamma}}/\partial \bar{\Gamma}): \bar{\Gamma} = I_1^{\bar{\Gamma}}, (\partial J_2^{\bar{\Gamma}}/\partial \bar{\Gamma}): \bar{\Gamma} = 2\,J_2^{\bar{\Gamma}}$ and $(\partial J_3^{\bar{\Gamma}}/\partial \bar{\Gamma}): \bar{\Gamma} = 3\,J_3^{\bar{\Gamma}}$ have been used here. The plastic multiplier is non-negative per definition. In addition, the terms in the bracket are non-negative as well, since the derivative of a convex, non-negative, and zero-valued function evaluated at a point x and the point x itself have the same sign. Conclusively, the reduced dissipation inequality is fulfilled for all n which proves thermodynamical consistency.

3. Neural Networks

The previous section has given insights into the mechanical preliminaries of the constitutive model. In the following, we present the structure of our iCANN which is based on these findings. The structure of the iCANN is held analogous to the one in Holthusen et al. (2023a) which includes a combination of a recurrent neural network (RNN) with feed-forward networks (FFN) for the elastic energy and the plastic potentials. As we have additively decomposed the energy into an elastic and a plastic term (c.f. Equation (13)), we learn two separate FFNs. In addition, plastic material behavior will be trained on two FFNs for the case of non-associative plasticity where the one describes the onset of plasticity through the yield function, whereas the second one defines the evolution of plastic stretches by the flow rule. In total, a set of the following four FFNs can be defined:

- ψ_e elastic Helmholtz free energy
- ψ_p plastic Helmholtz free energy to account for kinematic hardening
- \bullet h plastic potential defining the stress-dependent part of the yield surface
- g plastic potential defining the inelastic strain evolution

For associative plasticity, we obtain g = h and the set of FFNs reduces to three. Excluding hardening effects further reduces the number of trainable networks to two.

3.1. General network structure

The network structure is called in each time step and the input quantities are strain data, more specifically, the right Cauchy-Green components. Through the hidden states, the history variables are passed to ensure history-dependent material behavior. From these quantities, the input quantities for the FFNs, \vec{C}_e , C_p and $\bar{\Gamma}$, are computed. In an explicit integration scheme, the stress quantities of the last time step t_n are derived from which the plastic stretch of the current time step, $U_{p_{n+1}}$ is obtained. This one is then used, together with the current deformation state, C_{n+1} , to obtain the stress quantities from the networks of the energies and evaluate the Karush-Kuhn-Tucker conditions of the current time step. If the found stress state lies within the admissible solution, the second Piola-Kirchhoff stress, S, serves as the output quantity of the total network. The restriction to an admissible set of stress states differs from the original iCANN structure as it requires an additional iteration procedure which will be discussed in more detail in Section 4. Remark should be made, that the general form of the iCANN is chosen similarly to the energy and potential formulation used in Holthusen et al. (2023a). What is interesting to note, is that the approach given therein is held general such that the extension to plasticity made here is generally straightforward. However, the main difference lies in the treatment of inelastic effects as the predicted potential is not only used to describe an inelastic flow rule but also the admissible region and onset of inelastic effects. The latter one results in the different numerical treatment. Due to the previously described structure of the networks, a physically reasonable answer is ensured. In each call of the RNN, the networks for the energies and the potentials are called using the same set of weights respectively such that a unique answer is found.

3.2. Feed-forward networks for the Helmholtz free energy

The Helmholtz free energy will be derived by two feed-forward networks for the elastic and plastic part. Both are designed in analogy to the ones in (Linka et al., 2021), (Linka and Kuhl, 2023) and (Holthusen et al., 2023a). For the elastic energy, the co-rotated elastic right-Cauchy-Green deformation tensor, \bar{C}_e , serves as input from which its basic invariants $I_1^{\bar{C}_e}$, $I_2^{\bar{C}_e}$ and $I_3^{\bar{C}_e}$ are formulated. Decomposition into isochoric and volumetric terms and evaluation at the initial state leads to the first layer of the network pictured in orange

in Figure 2. The red layer follows from the Taylor series evaluation (c.f. Equation (11)) such that linear and quadratic forms are included, whereas in the last step (turquoise layer) linear and exponential activation functions are applied which are monotonic, continuous, and both, continuous differentiable and zero-valued at the origin. In addition, they are unbounded such that the growth criterion is fulfilled (c.f. Linka and Kuhl (2023)). The volumetric term is designed following Ogden (1972), such that the elastic Helmholtz free energy reads

$$\psi_{e}(\bar{C}_{e}) = w_{2,1}^{\psi_{e}} (\tilde{I}_{1}^{\bar{C}_{e}} - 3) + w_{2,2}^{\psi_{e}} \left(\exp(w_{1,2}^{\psi_{e}} [\tilde{I}_{1}^{\bar{C}_{e}} - 3]) - 1 \right)
+ w_{2,3}^{\psi_{e}} (\tilde{I}_{1}^{\bar{C}_{e}} - 3)^{2} + w_{2,4}^{\psi_{e}} \left(\exp\left(w_{1,4}^{\psi_{e}} [\tilde{I}_{1}^{\bar{C}_{e}} - 3]^{2} \right) - 1 \right)
+ w_{2,5}^{\psi_{e}} (\tilde{I}_{2}^{\bar{C}_{e}} - 3\sqrt{3}) + w_{2,6}^{\psi_{e}} \left(\exp(w_{1,6}^{\psi_{e}} [\tilde{I}_{2}^{\bar{C}_{e}} - 3]) - 1 \right)
+ w_{2,7}^{\psi_{e}} (\tilde{I}_{2}^{\bar{C}_{e}} - 3\sqrt{3})^{2} + w_{2,8}^{\psi_{e}} \left(\exp\left(w_{1,8}^{\psi_{e}} [\tilde{I}_{2}^{\bar{C}_{e}} - 3]^{2} \right) - 1 \right)
+ w_{3,2}^{\psi_{e}} \underbrace{\left[\left(\tilde{I}_{3}^{\bar{C}_{e}} \right)^{w_{3,1}^{\psi_{e}}} - 1 - w_{3,1}^{\psi_{e}} \ln\left(\tilde{I}_{3}^{\bar{C}_{e}} \right) \right]}_{W_{3}^{\bar{C}_{e}}}, \tag{20}$$

For the terms which are linear in both layers (red and turquoise), the set of weights has been reduced by all redundant weights. Hence, a total number of 14 weights result for this network. The weights of the first layer are controlling the shape of the activation functions whereas the ones of the second layer influence the total contribution of the layer to the final formulation of ψ_e . From Equation (20), the second Piola-Kirchhoff stress is derived according to Equation (7).

The previously described constraints can be applied on both, the elastic and plastic definition of the Helmholtz free energy. Therefore, the contribution corresponding to kinematic hardening, which describes the translation of the yield surface in the stress space without affecting its shape, is defined in analogy to the elastic term while the plastic right Cauchy-Green deformation serves as input here (see Figure 2 for $A = C_p$ and $a = \psi_p$). Again, the network is not fully connected to ensure polyconvexity.

$$\psi_{p}(C_{p}) = w_{2,1}^{\psi_{p}} (\tilde{I}_{1}^{C_{p}} - 3) + w_{2,2}^{\psi_{p}} \left(\exp(w_{1,2}^{\psi_{p}} [\tilde{I}_{1}^{C_{p}} - 3]) - 1 \right)$$

$$+ w_{2,3}^{\psi_{p}} (\tilde{I}_{1}^{C_{p}} - 3)^{2} + w_{2,4}^{\psi_{p}} \left(\exp\left(w_{1,4}^{\psi_{p}} [\tilde{I}_{1}^{C_{p}} - 3]^{2} \right) - 1 \right)$$

$$+ w_{2,5}^{\psi_{p}} (\tilde{I}_{2}^{C_{p}} - 3) + w_{2,6}^{\psi_{p}} \left(\exp(w_{1,6}^{\psi_{p}} [\tilde{I}_{2}^{C_{p}} - 3]) - 1 \right)$$

$$+ w_{2,7}^{\psi_{p}} (\tilde{I}_{2}^{C_{p}} - 3)^{2} + w_{2,8}^{\psi_{p}} \left(\exp\left(w_{1,8}^{\psi_{p}} [\tilde{I}_{2}^{C_{p}} - 3]^{2} \right) - 1 \right)$$

$$+ w_{3,2}^{\psi_{p}} \underbrace{\left[\left(I_{3}^{C_{p}} \right)^{w_{3,1}^{\psi_{p}}} - 1 - w_{3,1}^{\psi_{p}} \ln\left(I_{3}^{C_{p}} \right) \right]}_{W_{2}^{C_{p}}}$$

$$(21)$$

All redundant weights are omitted. Having defined the plastic Helmholtz free energy, we can now derive the final form of the backstress, χ (c.f. Equation (7)). Training of the network will then reveal which terms of

the formulation are included to accurately capture the underlying hardening behavior.

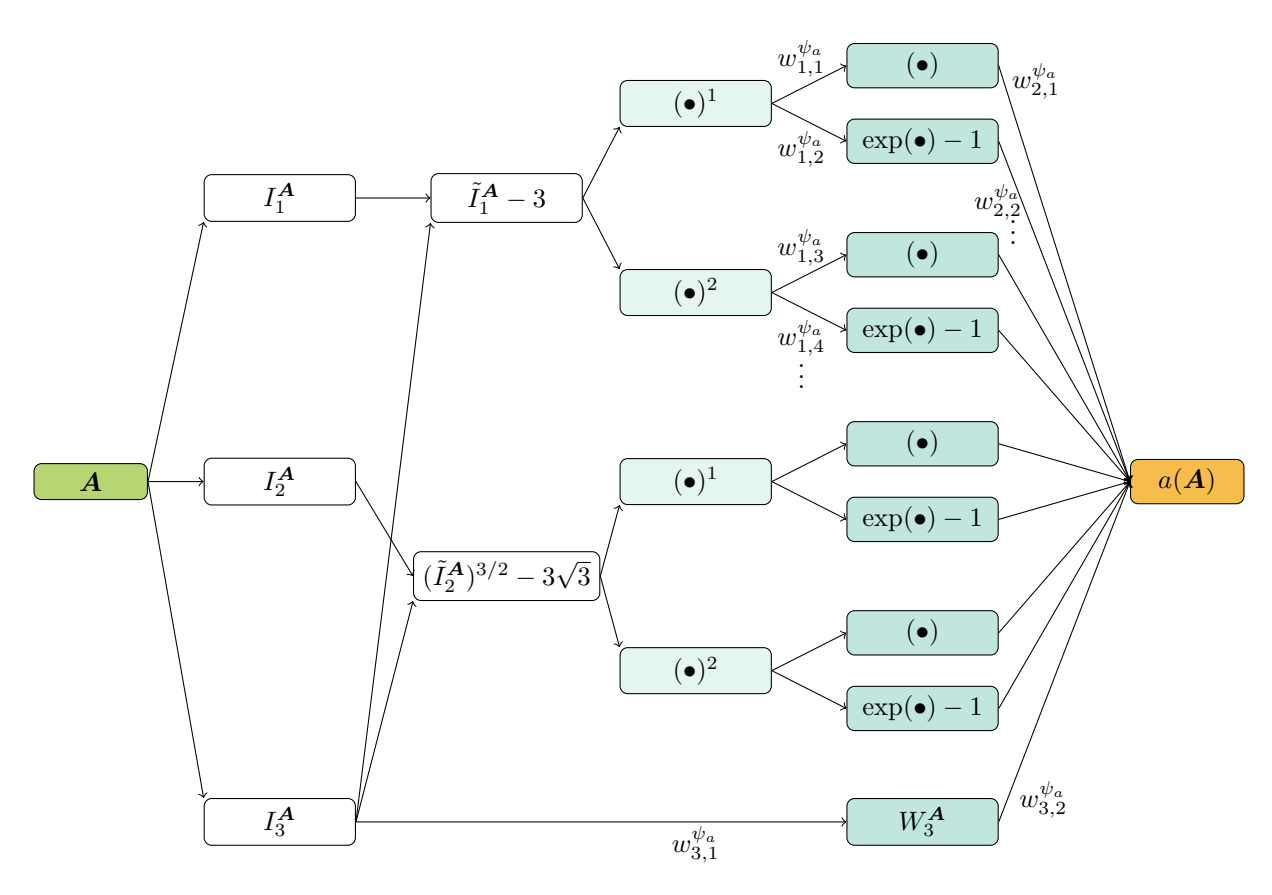


Figure 2: Schematic illustration of the feed-forward network of the elastic and plastic Helmholtz free energies. Elastic formulation: $\mathbf{A} = \bar{\mathbf{C}}_e$ and $a = \psi_e(\bar{\mathbf{C}}_e)$, plastic formulation: $\mathbf{A} = \mathbf{C}_p$ and $a = \psi_p(\mathbf{C}_p)$.

3.3. Feed-forward network for plastic potential

It remains to find a formulation for the plastic potential. Both potentials for the yield function and the plastic evolution must fulfill similar requirements. In consequence, the general structure of both potentials is similar. The relative stress, $\bar{\Gamma}$, serves as input quantity from which the invariants $I_1^{\bar{\Gamma}}$, $J_2^{\bar{\Gamma}}$ and $J_3^{\bar{\Gamma}}$ are formulated. The set of activation functions contains the absolute function, the natural logarithm of the hyperbolic cosine, and the hyperbolic cosine. These activation functions are continuous and continuous differentiable and by use of a not fully-connected network we ensure polyconvexity of the potential. The general structure of the network is illustrated in Figure 3. Similarly to the design of the Helmholtz free energies, we apply sets of weights controlling the shape of the activation functions and their contribution,

such that the potential reads

$$\begin{split} g(\bar{\Gamma}) &= w_{2,1}^g \operatorname{abs}\left(I_1^{\bar{\Gamma}}\right) + w_{2,2}^g \ln\left[\cosh\left(w_{1,1}^g I_1^{\bar{\Gamma}}\right)\right] + w_{2,3}^g \left[\cosh\left(w_{1,2}^g I_1^{\bar{\Gamma}}\right) - 1\right] \\ &+ w_{2,4}^g \operatorname{abs}\left((I_1^{\bar{\Gamma}})^2\right) + w_{2,5}^g \ln\left[\cosh\left(w_{1,2}^g (I_1^{\bar{\Gamma}})^2\right)\right] + w_{2,6}^g \left[\cosh\left(w_{1,4}^g (I_1^{\bar{\Gamma}})^2\right) - 1\right] \\ &+ w_{2,7}^g \operatorname{abs}\left(J_2^{\bar{\Gamma}}\right) + w_{2,8}^g \ln\left[\cosh\left(w_{1,3}^g J_2^{\bar{\Gamma}}\right)\right] + w_{2,9}^g \left[\cosh\left(w_{1,6}^g J_2^{\bar{\Gamma}}\right) - 1\right] \\ &+ w_{2,10}^g \operatorname{abs}\left((J_2^{\bar{\Gamma}})^2\right) + w_{2,11}^g \ln\left[\cosh\left(w_{1,5}^g (J_2^{\bar{\Gamma}})^2\right)\right] + w_{2,12}^g \left[\cosh\left(w_{1,8}^g (J_2^{\bar{\Gamma}})^2\right) - 1\right] \\ &+ w_{2,13}^g \operatorname{abs}\left(J_3^{\bar{\Gamma}}\right) + w_{2,14}^g \ln\left[\cosh\left(w_{1,7}^g J_3^{\bar{\Gamma}}\right)\right] + w_{2,15}^g \left[\cosh\left(w_{1,10}^g J_3^{\bar{\Gamma}}\right) - 1\right] \\ &+ w_{2,16}^g \operatorname{abs}\left((J_3^{\bar{\Gamma}})^2\right) + w_{2,17}^g \ln\left[\cosh\left(w_{1,9}^g (J_3^{\bar{\Gamma}})^2\right)\right] + w_{2,18}^g \left[\cosh\left(w_{1,10}^g J_3^{\bar{\Gamma}}\right) - 1\right]. \end{split} \tag{22}$$

By the design of the yield function in Equation (14), we can assume the weights of the potential of the yield function as scaled by the initial yield stress σ_{y_0} , such that $w_{i,j}^g = 1/\sigma_{y_0} \hat{w}_{i,j}^g$. By the choice of these activation functions, we automatically fulfill the p-norm regularization with p=1 as all activation functions are convex and non-negative. Therefore, taking the absolute of each function as stated in Equation (16) is redundant. Finally, all networks are described by physically reasonable quantities which can directly be computed. Therefore, the definition of the described constitutive artificial neural network will lead to reasonable results predicting elastic and non-associative plastic material behavior including hardening effects. It can easily be reduced by excluding hardening effects or capture associative plasticity.

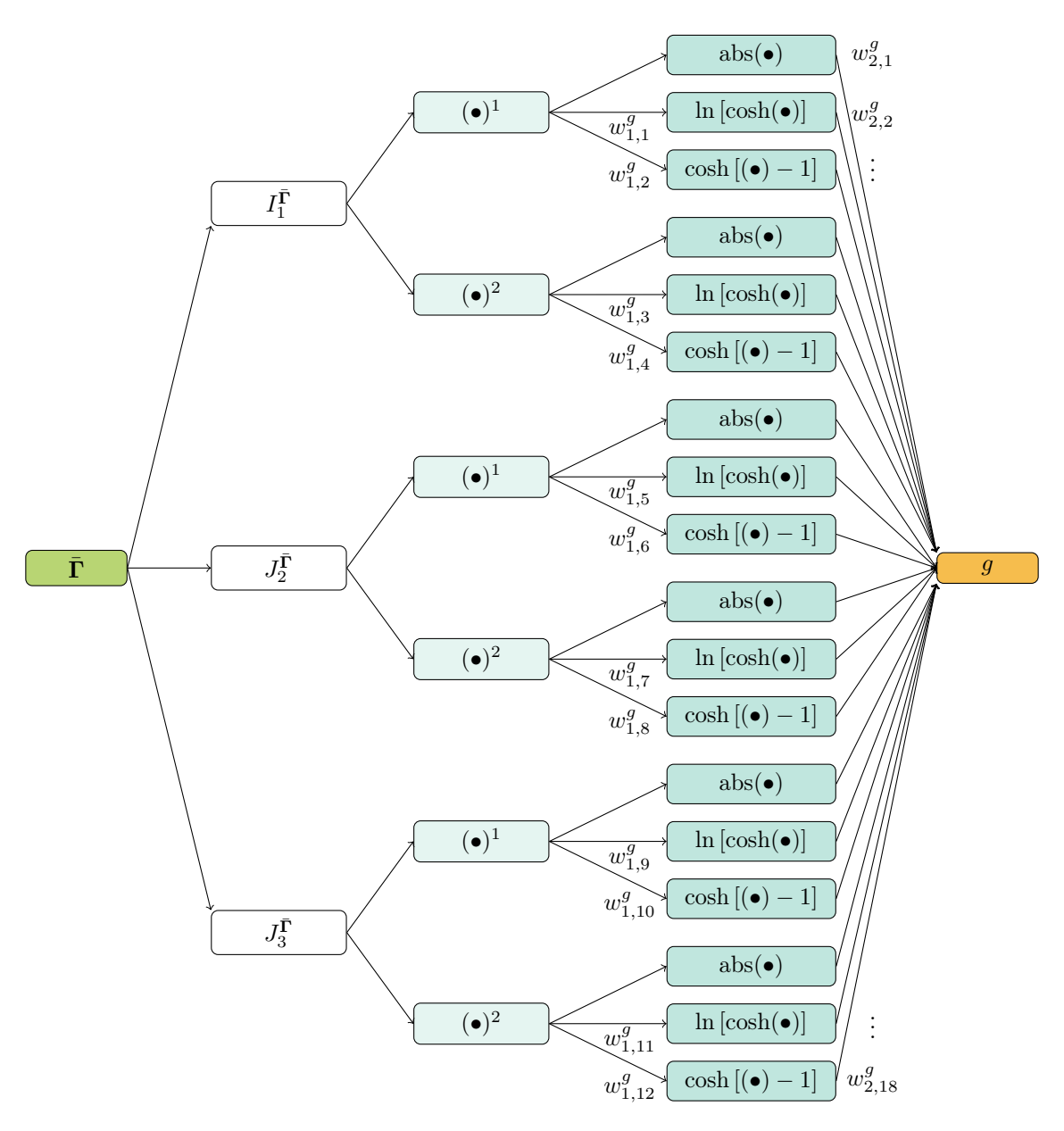


Figure 3: Schematic illustration of the feed-forward network of the plastic potential of Equation (22).

4. Specialization and numerical implementation of the general model

In the previous chapters, we have described the general design and the underlying theory of an inelastic constitutive neural network for elasto-plastic material behavior. To demonstrate its performance by numerical results, we will focus on a more specific formulation and give some details on the implementation in the following.

The framework is implemented into the open-source library *TensorFlow* (Abadi et al. (2016)). The iCANN is trained using the mean squared error – the difference of the experimental and predicted stresses – as the loss function, which is defined by

$$MSE = \frac{1}{n_{\text{data}}} \sum_{i=1}^{n_{\text{data}}} \left(\hat{S}_{11_i} - S_{11_i} \right)^2 \tag{23}$$

where \hat{S}_{11_i} is the first entry of the second Piola-Kirchhoff stress of the experimental data at step i and S_{11_i} is the predicted value.

4.1. Specialization of the Helmholtz free energies

We restrict this work to the class of incompressible material behavior. Therefore, we add a Lagrangian term to the energy, such that the total Helmholtz free energy is defined by $\psi = \psi_e + \psi_p + p(I_3^{\bar{C}_e}I_3^{\bar{C}_p} - 1)$. Here, p can be interpreted as the hydrostatic pressure that is computed from the boundary conditions. As we are considering coaxial loads only, it is defined such that $S_{33} = 0$ holds. The coaxial loads taken into account are uniaxial tension and compression ($C = \text{diag}[C_{11}, 1/\sqrt{C_{11}}, 1/\sqrt{C_{11}}]$), equibiaxial tension ($C = \text{diag}[C_{11}, C_{11}, 1/C_{11}]$) and pure shear ($C = \text{diag}[C_{11}, 1, 1/C_{11}]$). The elastic energy formulation has been described in Equation (20). To maintain a consecutive numbering of weights, we rewrite

$$\psi_{e}(\bar{C}_{e}) = w_{2,1}^{\psi_{e}} (\tilde{I}_{1}^{\bar{C}_{e}} - 3) + w_{2,2}^{\psi_{e}} \left(\exp(w_{1,1}^{\psi_{e}} [\tilde{I}_{1}^{\bar{C}_{e}} - 3]) - 1 \right)
+ w_{2,3}^{\psi_{e}} (\tilde{I}_{1}^{\bar{C}_{e}} - 3)^{2} + w_{2,4}^{\psi_{e}} \left(\exp\left(w_{1,2}^{\psi_{e}} [\tilde{I}_{1}^{\bar{C}_{e}} - 3]^{2} \right) - 1 \right)
+ w_{2,5}^{\psi_{e}} (\tilde{I}_{2}^{\bar{C}_{e}} - 3) + w_{2,6}^{\psi_{e}} \left(\exp(w_{1,3}^{\psi_{e}} [\tilde{I}_{2}^{\bar{C}_{e}} - 3]) - 1 \right)
+ w_{2,7}^{\psi_{e}} (\tilde{I}_{2}^{\bar{C}_{e}} - 3)^{2} + w_{2,8}^{\psi_{e}} \left(\exp\left(w_{1,4}^{\psi_{e}} [\tilde{I}_{2}^{\bar{C}_{e}} - 3]^{2} \right) - 1 \right)
+ w_{3,2}^{\psi_{e}} \underbrace{\left[\left(I_{3}^{\bar{C}_{e}} \right)^{-w_{3,1}^{\psi_{e}}} - 1 + w_{3,1}^{\psi_{e}} \ln\left(I_{3}^{\bar{C}_{e}} \right) \right]}_{W_{3}^{\bar{C}_{e}}}, \tag{24}$$

Due to a limited data availability, we aim to reduce the number of weights in the plastic Helmholtz free energy and consider linear components only. This is considered to be sufficient as we want to prove the general capacity to model hardening effects with a limited amount of data. Thus, strongly non-linear and the volumetric terms are neglected here. The plastic Helmholtz free energy then includes six additional weights and reads

$$\psi_{p}(C_{p}) = w_{2,1}^{\psi_{p}} (\tilde{I}_{1}^{C_{p}} - 3) + w_{2,2}^{\psi_{p}} \left(\exp(w_{1,1}^{\psi_{p}} [\tilde{I}_{1}^{C_{p}} - 3]) - 1 \right)$$

$$+ w_{2,3}^{\psi_{p}} (\tilde{I}_{2}^{C_{p}} - 3) + w_{2,4}^{\psi_{p}} \left(\exp(w_{1,2}^{\psi_{p}} [\tilde{I}_{2}^{C_{p}} - 3]) - 1 \right)$$

$$+ w_{3,2}^{\psi_{p}} \left[\left(I_{3}^{C_{p}} \right)^{w_{3,1}^{\psi_{p}}} - 1 - w_{3,1}^{\psi_{p}} \ln \left(I_{3}^{C_{p}} \right) \right]$$

$$(25)$$

4.2. Specialization of the plastic potentials

For most practical purposes, it is sufficient to describe the yield surface in terms of the first and second deviatoric invariants, $I_1^{\bar{\Gamma}}$ and $J_2^{\bar{\Gamma}}$ as the influence of $J_3^{\bar{\Gamma}}$ on the results for isotropic materials is often negligible (Hill (1952)). Following (Taç et al., 2023) and (Holthusen et al., 2023a), we choose a set of $I_1^{\bar{\Gamma}}$, $(I_1^{\bar{\Gamma}})^2$ and $J_2^{\bar{\Gamma}}$, and neglect any terms considering the third deviatoric invariant for simplicity and computational efficiency. For more complex yielding behavior such as an observable tension-compression asymmetry, for example, this term could be included and compensated by an extended set of training data. To further reduce the number of weights, we consider only one single yield surface by setting n=1 in Equation (18). Ensuring convexity, we choose p=1 in Equation (16). Conclusively, a smooth boundary of the potentials is ensured such that numerical problems during computation of the flow rule are prevented. Thus, the following plastic potential, g, is used throughout this work, i.e.

$$g(\bar{\Gamma}) = w_{2,1}^g \operatorname{abs} \left(I_1^{\bar{\Gamma}} \right) + w_{2,2}^g \ln \left[\cosh \left(w_{1,1}^g I_1^{\bar{\Gamma}} \right) \right]$$

$$+ w_{2,3}^g \operatorname{abs} \left((I_1^{\bar{\Gamma}})^2 \right) + w_{2,4}^g \ln \left[\cosh \left(w_{1,2}^g (I_1^{\bar{\Gamma}})^2 \right) \right]$$

$$+ \tilde{w}_{2,5}^g \operatorname{abs} \left(\tilde{J}_2^{\bar{\Gamma}} \right) + w_{2,6}^g \ln \left[\cosh \left(\tilde{w}_{1,3}^g \tilde{J}_2^{\bar{\Gamma}} \right) \right].$$
(26)

In line with (Taç et al., 2023; Holthusen et al., 2023a), the second deviatoric invariant has been scaled by $\tilde{J}_2^{\bar{\Gamma}} = 3J_2^{\bar{\Gamma}}$ such that $\tilde{w}_{2,1}^g = 1/3\,w_{2,1}^g$ and $\tilde{w}_{1,3}^g = 1/3\,w_{1,3}^g$ holds.

Together with the elastic and plastic Helmholtz free energies in Equations (24) and (25), all equations of the model have been defined. In total, this leads to a number of 14 + 6 + 9 = 23 weights for a single-surface plasticity model.

4.3. Time discretization

The evolution equation is discretized in a time interval $t \in [t_n, t_{n+1}]$, and an explicit time integration scheme is used. For this, an exponential integration scheme is applied, such that the plastic evolution yields $C_{p_{n+1}} = U_{p_n} \exp(2 \Delta \lambda \bar{D}_p) U_{p_n}$ with $\Delta \lambda := \Delta t \dot{\lambda}$. This form ensures the plastic incompressibility condition of $\det(C_{p_{n+1}}) = 1$. The explicit integration is schematically given in Figure 4, which depicts the structure of the recurrent neural network called at each time step. The Helmholtz free energy, plastic potentials, and all stress quantities from the time step t_n are computed first. From this, the plastic stretches are updated

explicitly, and all quantities of the current time step t_{n+1} are computed by an elastic trial step, which is indicated by the blue box in Figure 4. Including plasticity into the framework requires fulfillment of the loading-unloading conditions. If these conditions are not met, a plastic corrector iteration is performed, which will be described in more detail in the following section. The explicit integration scheme and the iteration procedure lead to several calls of the network(s) of the Helmholtz free energy and the potentials. However, it should be noted, that in each call, the weights of the corresponding network are the same such that a unique set of weights is trained for each network. While the Newton-Raphson iteration is performed, the feed-forward networks are called for every iteration step but, again, the same sets of weights are used. In addition, the weights for the network of the yield function and of the plastic potential are the same for the case of associative plasticity. Thus, this choice leads to a decreased number of trainable weights which might be advantageous for limited data availability.

4.4. Elastic predictor-plastic corrector scheme

Having discretized the evolution equation, we focus on the implementation of plasticity. As stated in Section 2, the yield surface encloses all admissible stress states. This restriction results from introducing plasticity effects into the framework of iCANNs which brings us to using an elastic predictor-plastic corrector algorithm. Thus, we explicitly update the inelastic stretches and set $\Delta\lambda=0$, i.e. assuming elastic material behavior in a trial step. With this, the trial stresses are computed and it is checked if our trial state is plastically admissible (c.f. the blue box in Figure 4). If this is the case, the elastic trial case is accepted as solution. Otherwise, a plastic corrector step is applied which enforces plastic admissibility. An iterative procedure to find an admissible solution is performed. We use the common approach of a Newton-Raphson scheme. As depicted in Figure 4 in the turquoise box, the plastic multiplier is iteratively updated by $\Delta\lambda=-(\partial r/\partial x)^{-1}r$, where $r=\Phi$ is the residual to be minimized and x are the internal variables, which are the plastic multiplier in this case.

In comparison to the existing iCANNs, the application of the predictor-corrector scheme is a novel extension such that the class of inelastic effects captured is extended. With this, a wider class of materials can be captured by the predictive tool of constitutive artificial neural networks.

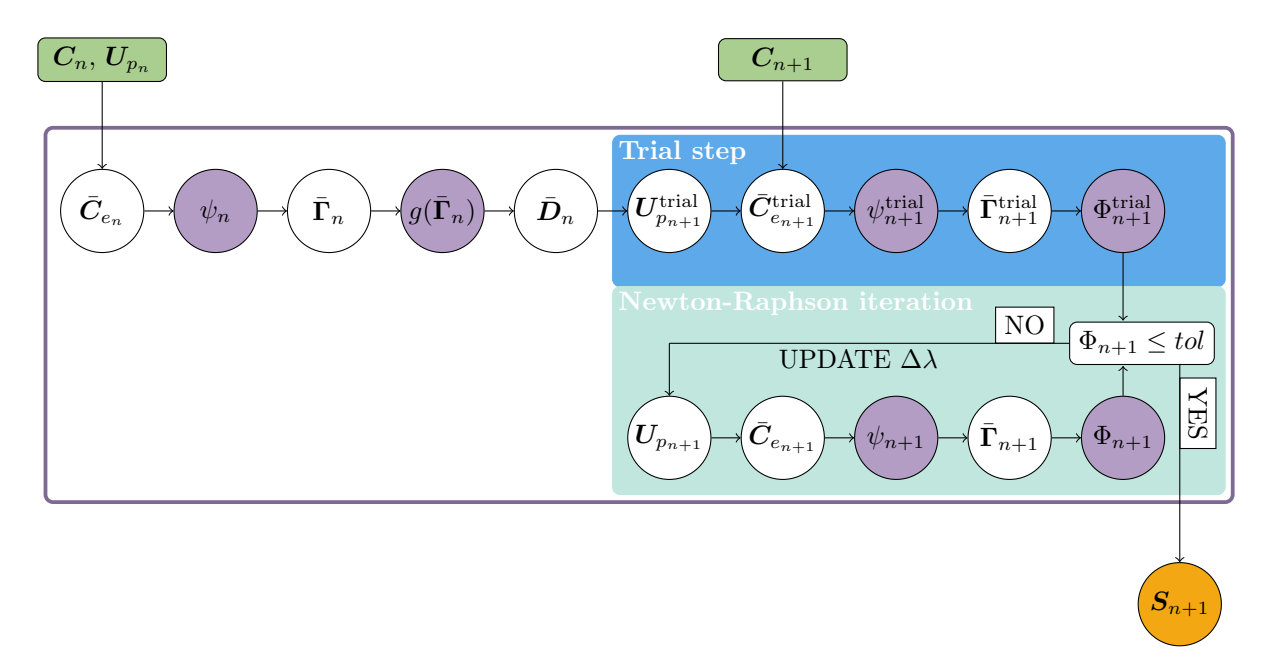


Figure 4: Structure of the recurrent neural network (purple square): Inputs are the right Cauchy-Green tensor and the plastic stretch from the last time step n. Elastic trial step pictured in blue box and Newton-Raphson iteration in the turquoise box. Filled purple circles indicate call of the corresponding feed-forward networks.

5. Results

The previously described framework presents a new class of iCANNS to find material models capturing plastic material behavior. In the following, numerical results are demonstrated to validate the presented framework of neural networks to predict different plastic behaviors. We began with artificially generated data of a perfect plasticity model and investigated the required loading cases to accurately find the most suitable weights. Then, stress-strain data that included tension-compression asymmetry were artificially generated and used as training data to analyze the prediction of the iCANN for material phenomena that could not be captured by the current formulation. While the first two data sets captured perfect plasticity, an additional data set that included kinematic hardening was then used to study the behavior under more complex behavior where the additional network of the plastic energy formulation in Equation (21) came into account. Finally, experimental data of Kowalewski et al. (2014) were used to investigate the performance on real data.

Throughout all results, the ADAM optimization has been used. If not mentioned otherwise, L2-regularization has been applied with $L_2 = 0.001$.

5.1. Perfect plasticity - artificially generated data

Perfect plasticity was first investigated such that the model prediction on the onset of plasticity was in focus. All hardening terms were neglected here, and associative plasticity was chosen. Different sets of training data were used and their influence on the predicted model was investigated. The data sets consisted of artificially created data from a classical incompressible Neo-Hookean type material model with a yield criterion of von Mises-type. The training data was generated by

$$\psi(\bar{\boldsymbol{C}}_e) = \frac{\mu}{2} \left(\frac{\operatorname{tr}(\bar{\boldsymbol{C}}_e)}{\det(\bar{\boldsymbol{C}}_e)^{1/3}} - 3 \right) + \frac{K}{4} \left(\det(\bar{\boldsymbol{C}}_e) - 1 - \ln[\det(\bar{\boldsymbol{C}}_e)] \right) - p \left(I_3^{\boldsymbol{C}} - 1 \right)$$
 (27)

as the Helmholtz free energy. The last term was added as a Lagrange term where p was the hydrostatic pressure and was derived from the boundary conditions. The yield function was defined by

$$\Phi(\bar{\Gamma}) = \frac{3}{2} \operatorname{tr} \left(\operatorname{dev}(\bar{\Gamma})^2 \right) - \sigma_{y_0}^2$$
(28)

The material parameters used were the shear modulus $\mu = 12.5$ kPa, bulk modulus K = 25 kPa and the yield stress $\sigma_{y_0} = 2$ kPa. The specific form of Equation (28) could be captured by the designed network in Equation (26) for $w_{2,5}^g = 0.25$. Therefore, it was interesting to investigate under which loading scenarios an accurate prediction was made. We considered loading scenarios of uniaxial tension (UT), uniaxial compression (UC), equibiaxial compression (EB), pure shear (PS) and uniaxial cyclic loading as described in Section 4. These data sets were used in five different combinations to examine the model prediction with different training data. The five sets were (UT), (UT, UC), (UT, EB), (UT, UC, EB), and (UT, UC, EB, S). Every training has been performed with a number of 5000 epochs, even though convergence could be assumed after 1000 epochs already (see Figure 6 (f)).

The predicted weights of the plastic potential are given in Table 1 for all five training sets. For the training on uniaxial tension, we observed some weights being equal or already close to zero. However, with an increasing number of loading sets, the number of active weights decreased, whereas for the last set of four loading sets, the predicted solution has converged to the actual solution. We recall here the interpretation of the weights divided by the initial yield stress such that we could compare the obtained weight $w_{2,5}^g$ with the squared initial yield stress in Equation (28). Regarding the specific weights of the yield function, more training data led to better prediction of the underlying material behavior.

However, the predicted yield surface did not differ qualitatively as plotted in Figure 5 where the yield surface at the $\sigma_1 - \sigma_2$ -plane is given. The blue solid line indicates the model that is trained on whereas the four black markers represent the yield stresses of the four loading scenarios of UT, UC, EB, and PS. Comparing the predicted yield surface trained on UT (orange, dashed line) and the one trained one UT, UC, EB and S (purple dotted), the results seemed similar, even though the first one includes more active activation functions. In conclusion, a wider set of training data leads to more precise results, but an already sufficient solution was observed for a minimum number of training data. In addition to the yield surface, the stress-strain data of the artificially generated data, and the model prediction trained on four loading sets are given in Figure 6 (a) to (e). The loss over the number of epochs is shown in Figure 6 (f). Further to Table 1, the predicted weights of the Helmholtz free energy are given in Table A.4.

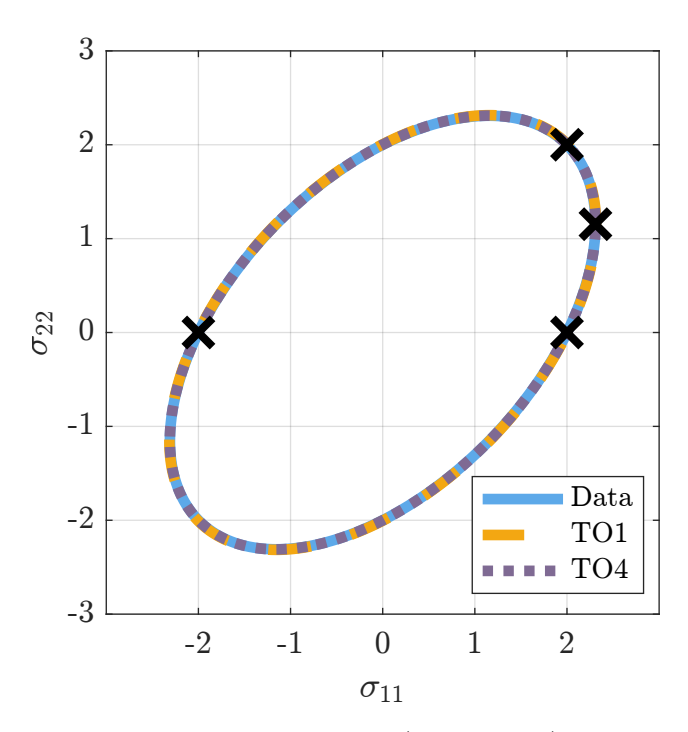


Figure 5: Yield function at $\sigma_{33} = 0$ for the artificially generated data (blue, solid line), model prediction trained on UT (orange, dashed line) and model prediction trained on UT, UC, EB, S (purple, dotted line). Black marks indicate the yield stresses of the four loading cases.

Table 1: Predicted weights of the plastic potential for perfect plasticity for the corresponding training sets presented in the headline (UT – uniaxial tension, UC – uniaxial compression, EB – equibiaxial tension, PS – pure shear).

	UT	UT, UC	UT, EB	UT, UC, EB	UT, UC, EB, PS
$w_{1,1}^{g}$	0	0	0	0	0
$w_{1,2}^{g}$	1.773e-21	0	0	0	0
$w_{1,3}^{g}$	0.3052	2.803e-28	7.866e-10	0	0
$w_{2,1}^{g}$	1.252e-6	9.352e-7	7.689e-7	5.533e-6	0
$w_{2,2}^{g}$	0	0	0	0	0
$w_{2,3}^{g}$	1.211e-11	7.226e-13	8.736e-12	0	0
$w_{2,4}^{g}$	7.790e-35	0	0	0	0
$w_{2,5}^{g}$	0.2200	0.2497	0.2497	0.2497	0.2498
$w_{2,6}^{g}$	0.1879	2.011e-5	1.658e-4	0	0

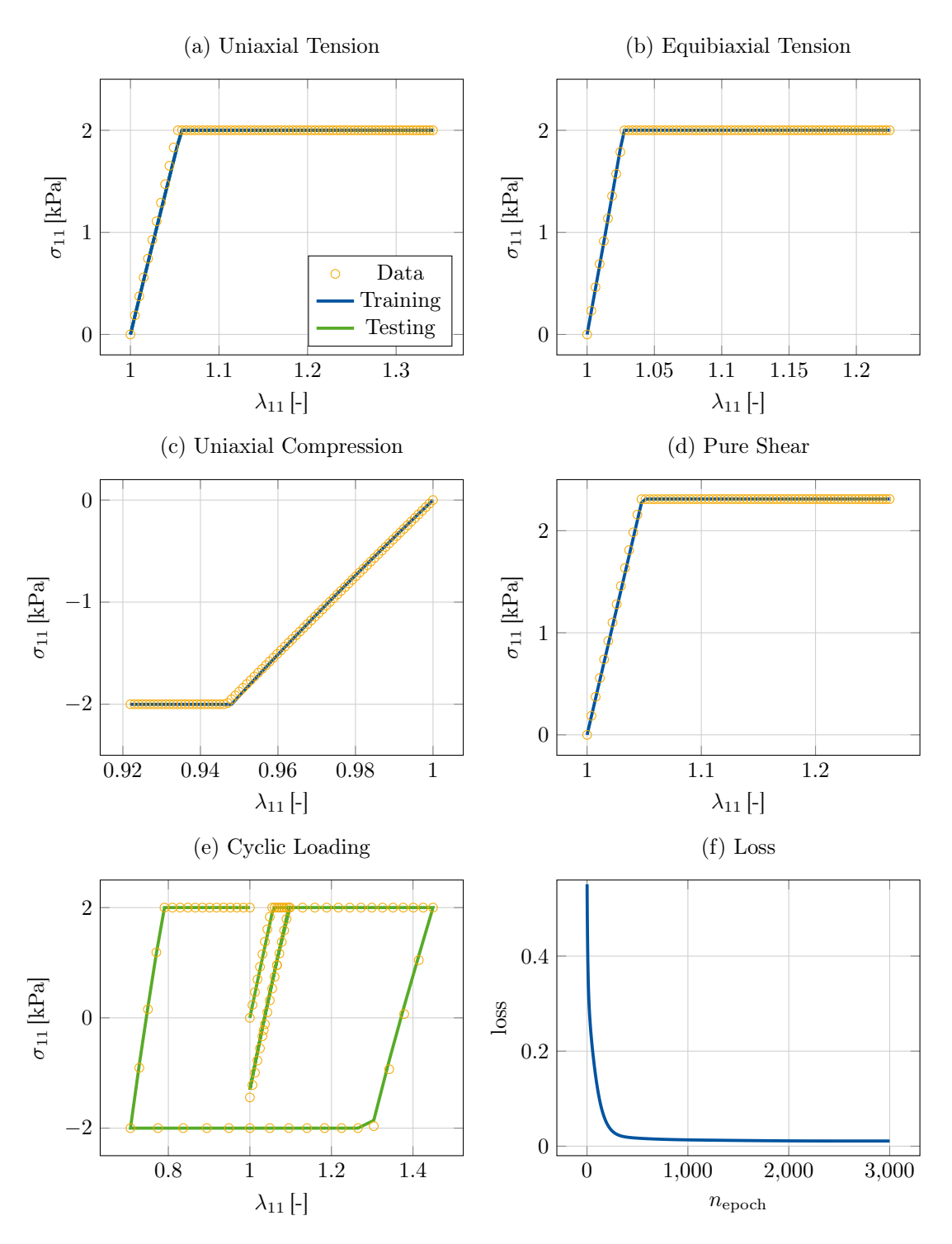


Figure 6: Perfect plasticity: Stress-strain curves of the artificially generated data (orange markers) and the trained (blue, solid) and tested (green, solid) model prediction for (a) uniaxial tension, (b) equibiaxial tension, (c) uniaxial compression, (d) Shear, (e) cyclic loading and (e) the corresponding loss curve.

5.2. Tension-compression asymmetry – artificially generated data

In comparison to the training data used above, it was interesting to investigate the model prediction trained on data that was not included in the structure of the iCANN. Thus, an artificially generated data set of en elasto-plastic material with tension-compression asymmetry was considered. We used a compressible Neo-Hookean type energy as in Equation (27) with p=0 with a paraboloid yield function presented by Tschoegl (1971) which reads

$$\Phi = 3J_2 + (\sigma_C - \sigma_T)I_1 - \sigma_C \sigma_T. \tag{29}$$

Here, we defined the initial yield stress in tension by $\sigma_T = 2$ MPa and in compression by $\sigma_C = 4$ MPa. Tension-compression asymmetry was captured through the sign of the first invariant I_1 . The used activation functions excluded any dependency of the sign as they were designed to be non-negative and convex. It was therefore obvious, that no solution could be found, which matched both tension and compression simultaneously. All sets were trained over 5000 epochs.

In a first step, we trained the network on uniaxial tension only. These training data did not give any information on the tension-compression asymmetry of the underlying material model and the found yield surface was of cylindrical form. The corresponding weights are given in Table 2 and could be interpreted as a von Mises-type yield criterion similar to the one in the previous Section. The predicted yield surface and the one of the artificially generated data were compared in Figure 7 (a) at the σ_{11} - σ_{22} -plane and in Figure 7 (b) in the three-dimensional stress space. The black marker indicated the yield stress of uniaxial tension. It could be seen clearly, that the yield stress trained on was perfectly met. In addition, the yield stress for uniaxial tension in the x_2 -direction was also met. However, the predicted yield surface did not match any other stress state of the given material model. Thus, the included elastic regime bounded by the yield surface differed from the one aimed to be fitted. In conclusion, one training set was not sufficient to predict the yield surface given in Equation (29).

Therefore, the training set was extended to uniaxial and biaxial tension. Regarding the weights of this training set in Table 2, we observed that a contribution of the first stress invariant, $I_1^{\bar{\Gamma}}$, was included in the predicted yield criterion. This influence was clearly visible in the visualization of the yield function in Figure 8. The predicted yield surface did not form a cylinder around the hydrostatic axis anymore but a symmetric spherical shape with its center at the origin. This symmetry revealed that any tension-compression asymmetry cannot be captured. However, the onset of plasticity in the tension regime was already adapted relatively fine.

Finally, uniaxial tension and uniaxial compression were given as training sets. As only symmetric results could be found, a yield criterion that predicted a yield stress of 3 kN would have be expected as it would meet the mean value between the yield stresses in tension and compression. However, the predicted yield surface in Figure 9 showed that a von Mises-type surface with a radius of 4 kN was found. Recalling the

Table 2: Perfect plasticity with tension-compression asymmetry: predicted weights for training on combinations of uniaxial tension (UT), uniaxial compression (UC) and equibiaxial tension (EB).

	UT	UT,EB	UT, UC	
$w_{1,1}^{g}$	0 0		0	
$w_{1,2}^{g}$	0	0	0	
$w_{1,3}^{g}$, ₃ 8.494e-8 0		0.3526	
$w_{2,1}^{g}$	3.325e-7	0.2981	1.467e-4	
$w_{2,2}^{g}$	0	0	0	
$w_{2,3}^{g}$	3.080e-12	0	4.903e-8	
$w_{2,4}^{g}$	0	0	0	
$w_{2,5}^{g}$	0.2496	0.1454	3.373e-2	
$w_{2,6}^{g}$	3.579e-2	0	9.340e-2	

computation of the loss in Equation (23), the second Piola-Kirchhoff stress was used as an error measure. While the Cauchy stress remained constant after the onset of plasticity (c.f. Figure 6 (a)), the second Piola-Kirchhoff stress decreased for uniaxial tension in the plastic regime and increased for uniaxial compression. Therefore, uniaxial compression was more significant and to reduce the total error of the model, the final solution found was oriented on the data of uniaxial compression. The corresponding weights of the yield surface were given in Table 2. All predicted weights of the elastic Helmholtz free energy were shown in Table A.5 for completeness.

5.3. Kinematic hardening – artificially generated data

To investigate hardening effects, the incompressible Neo-Hookean type material model of Equation (27) was extended by an additional hardening term of

$$\psi_p(\mathbf{C}_p) = \frac{c}{2} \left(\frac{\operatorname{tr}(\mathbf{C}_p)}{\det(\mathbf{C}_p)^{1/3}} - 3 \right)$$
(30)

with c=2 kN as a hardening parameter. The yield surface remained equal to Equation (28), and associative plasticity was modelled. The model was trained on uniaxial tension only with a number of 5000 epochs. We tested the performance of the predicted model using cyclic loading. The stress-strain curves in Figure 10 (a) and (b) qualitatively underlined the performance whereas the loss curve in Figure 10 (c) quantitatively indicated that our predicted results aligned well with the artificially generated data. Interestingly, the model was trained on stretch data up to a stretch of $\lambda_{11}=1.35$. However, it was tested up to larger stretches and, in addition, also by compressive loads which had not been used for training. This underlined the predictive possibilities even outside the trained regime. In contrast to unconstrained neural networks, this allowed us extrapolation beyond the trained data sets as the underlying neural network and model

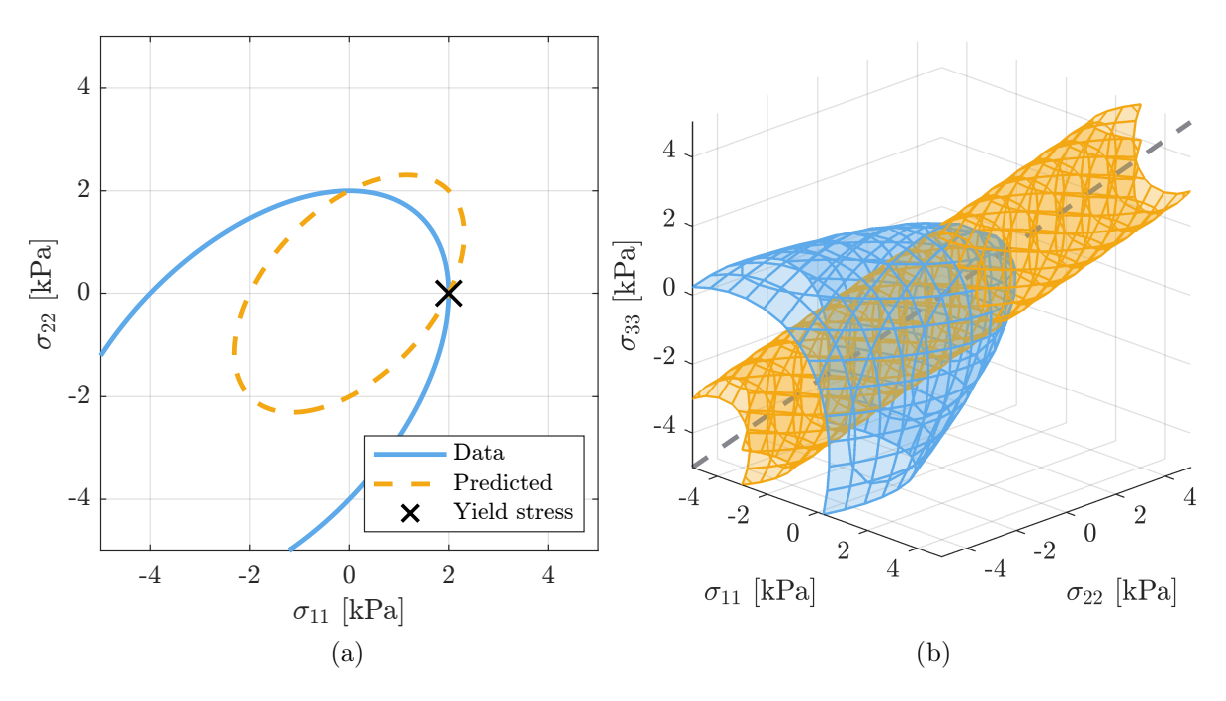


Figure 7: Trained on uniaxial tension: Yield function of the predicted model (orange, dashed) and of the artificially generated data (blue, solid) with the yield stress given in the training set (black marker): (a) in 2D at σ_{11} - σ_{22} -plane, (b) in 3D (hydrostatic axis is given for reference in grey).

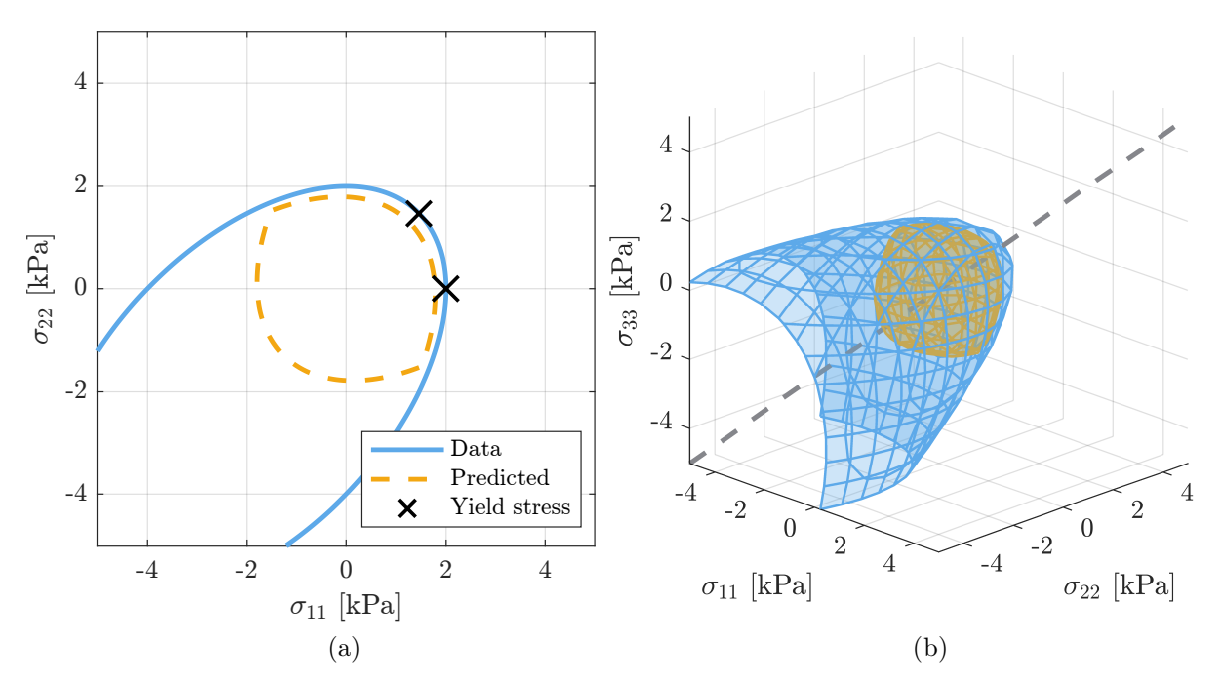


Figure 8: Trained on uniaxial tension and equibiaxial tension: Yield function of the predicted model (orange, dashed) and of the artificially generated data (blue, solid) with the yield stress given in the training set (black marker): (a) in 2D at σ_{11} - σ_{22} -plane, (b) in 3D (hydrostatic axis is given for reference in grey).

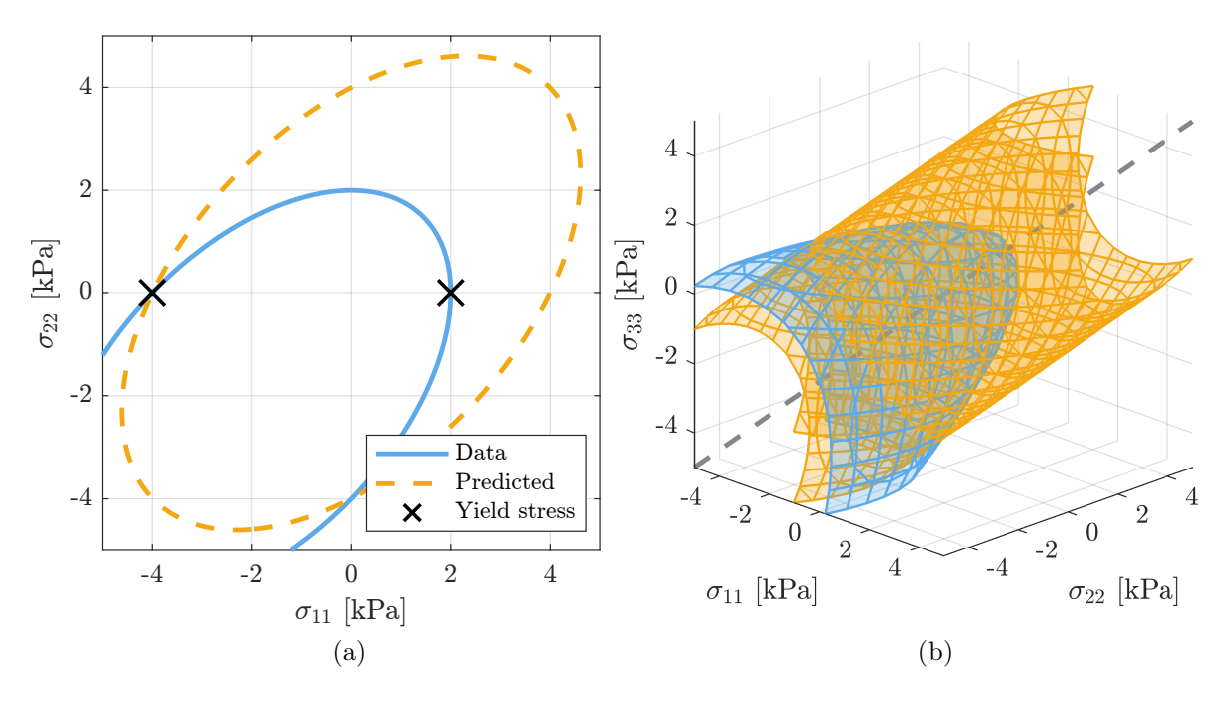


Figure 9: Trained on uniaxial tension and uniaxial compression: Yield function of the predicted model (orange, dashed) and of the artificially generated data (blue, solid) with the yield stress given in the training set (black marker): (a) in 2D at σ_{11} - σ_{22} -plane, (b) in 3D (hydrostatic axis is given for reference in grey).

was designed in a physically reasonable manner following the principle of kinematics, thermodynamics and material theory.

The corresponding weights of the predicted yield surface were given in Table 3. Similar to the results from the sections above, we almost met the von Mises-type yield surface as the most dominant weight was $w_{2,5}^g$. Perfect agreement would have been observed for $w_{2,5}^g = 0.25$. In addition, the predicted yield surface and the one of the artificially generated data showed a qualitatively good agreement, which was visualized in Figure 10 (d). The dashed curves represented both yield surfaces in the initial state. In addition, the translated yield surfaces after the maximum tensile loading (indicated by point A in Figure 10 (b)) were plotted by dotted lines. The hardening effect was mostly described by the linear and quadratic terms of the first invariant (c.f. Table 3). The found weights of $w_{2,1}^{\psi_p} = 0.6029$ and $w_{2,3}^{\psi_p} = 0.4852$ did not match to the one of the artificially generated data that would have been $w_{2,1}^{\psi_p} = 1$ for c = 2 kN. However, we observed the hardening behavior being described adequately as underlined by the stress-strain curves and the visualization of the initial and translated yield surfaces in Figure 10. Thus, the predicted hardening model translated the yield surfaces similarly compared to the one of the artificially generated data.

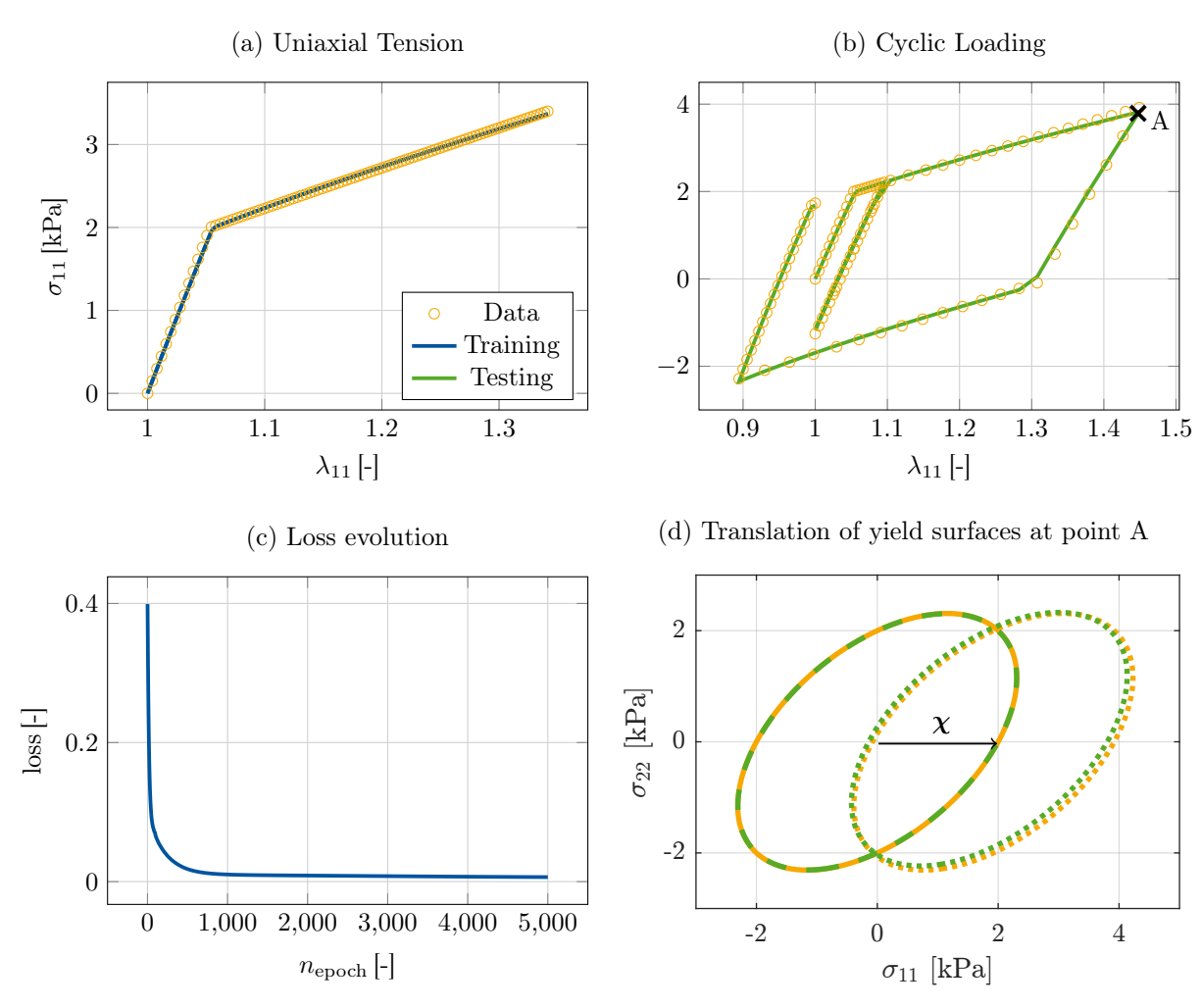


Figure 10: Plasticity with hardening effects: Stress-strain curves of the artificially generated data (orange markers) and the trained (blue, solid) and tested (green, solid) model prediction for (a) uniaxial tension and (b) cyclic loading. (c) Loss evolution over number of epochs for uniaxial tension. (d) Initial yield surfaces (dashed) and translated yield surfaces (dotted) of the trained data (orange) and predicted data (green) after maximum tensile loading (point A indicated in (b)). Translation of the center indicated by the backstress, χ .

Table 3: Kinematic hardening: predicted weights for training on uniaxial tension

i	g	ψ_p	ψ_e	
$w_{1,1}^{i}$	0.6023	0	0	
$w_{1,2}^i$	0.7530	0	0	
$w_{1,3}^{i}$	0.4079	-	0	
$w_{1,4}^{i}$	-	-	0	
$w_{2,1}^{i}$	3.505e-7	0.3006	1.4290	
$w_{2,2}^i$	0	0	0	
$w_{2,3}^{i}$	2.330e-12	0.3263	1.169e-2	
$w_{2,4}^i$	0	0	0	
$w_{2,5}^i$	0.2323	-	1.8390	
$w_{2,6}^{i}$	7.529e-2	-	0	
$w_{2,7}^i$	-	-	7.340e-2	
$w_{2,8}^{i}$	-	-	0	
$w_{3,1}^{i}$	-	7.493e-9	2.660e-8	
$w_{3,2}^{i}$	-	1.709	2.094	

5.4. Kinematic hardening – experimental data

Finally, the learning and prediction of the iCANN of experimental data was investigated. For this, experimental data of X10CrMoVNb9-1 steel from Kowalewski et al. (2014) were extracted from uniaxial tensile tests and cyclic tension-compression tests by extracting data points from their published graphs. The experimental stress-strain data were visualized in Figure 11 (a) for uniaxial tension and (b) for cyclic loading. Assuming incompressibility and small deformations, the data were transformed to the right Cauchy-Green tensor and the second Piola-Kirchhoff stress to serve as inputs for the model. The stress has been scaled by its maximum value before being given as input data into the network model and was rescaled after computation for visualization as this has simplified the training process. Following McCulloch et al. (2024), we performed a pre-training of the model to find start values that were already close to the final solution. This pre-training has been proven to be more efficient compared to a training with solely random initial weights. For the pre-training, we aimed to optimize the initial weights of the elastic Helmholtz free energy first and therefore set all weights to zero and non-trainable except for the ones referring to the elastic material behavior, i.e. all $w_{i,j}^{\psi_e}$ in Equation (20). We only trained the ones referring to the linear terms $-w_{2,1}^{\psi_e}, w_{2,3}^{\psi_e}, w_{2,5}^{\psi_e}$ and $w_{2,7}^{\psi_e}$. Then the remaining weights corresponding to the exponential function were trained separately. For both trainings a number of 10000 epochs and L_1 -regularization were used. The resulting weights were taken as starting points for training of the total elastic energy including now both, linear and exponential terms. Thereafter, initialization of the weights of the yield criterion was performed by setting the corresponding weights to be the only trainable ones and training of 1000 epochs with L_2 regularization with a factor of 0.001. Lastly, the found weights were set to non-trainable again and the weights corresponding to the hardening are trained on 1000 epochs again. With this pre-training, the initial weights used as a starting point for the real training process were already in the range of the final solution. This approach could be used as a general procedure for all constitutive neural networks and is less error-prone since the total range of the predicted model was already close to the final solution. In addition, this procedure was time efficient as in each pre-training step only a small number of weights were trained compared to the overall model which was computationally more efficient. The resulting weights which were used as starting points for the total training were given in Table A.6 for completeness.

We have trained the total model once on the uniaxial tensile data (blue solid line) and once on the cyclic tension-compression data (green solid line). Both, training and testing results, were visualized in Figure 11 (a) and (b) while the predicted data used for testing were indicated by dashed lines. Both loss curves were plotted in Figure 11 (c). For completeness, the predicted weights were given in Table A.7. Regarding the training on the uniaxial tensile data, it could be seen that the prediction on the cyclic loading was met closely in the first tensile loading applied. During the unloading in the compression regime and reloading, an offset was observable in the transition from elastic to plastic material behavior. In total, the general stress-strain curve was qualitatively met. The predicted model trained on the cyclic loading data in total fitted better to both data sets, uniaxial tension and cyclic loading. What should be noted were additional kinks in the transition from elastic to plastic behavior in the unloading and reloading phase in Figure 11 (b). It indicated the onset of yielding in between the two data points corresponding to the kinks. From this, we concluded that to accurately predict the yield stress of the underlying material, enough data points in the regime where a transition into the plastic regime was expected should be considered. Then, the network model would get precise information about the onset of yielding. Thus, when producing experimental data, we should take this observation into account.

6. Conclusion and outlook

This work deals with constitutive artificial neural networks, which allow finding physically reasonable, new material models. These networks learn material models that a priori include the underlying principles and constraints of continuum mechanics such as objectivity, material symmetry, capture rigid motions of the reference configuration, rotational non-uniqueness, and fulfill thermodynamic consistency. This leads to the development of physically sound material models that can predict material behavior even outside the trained regime.

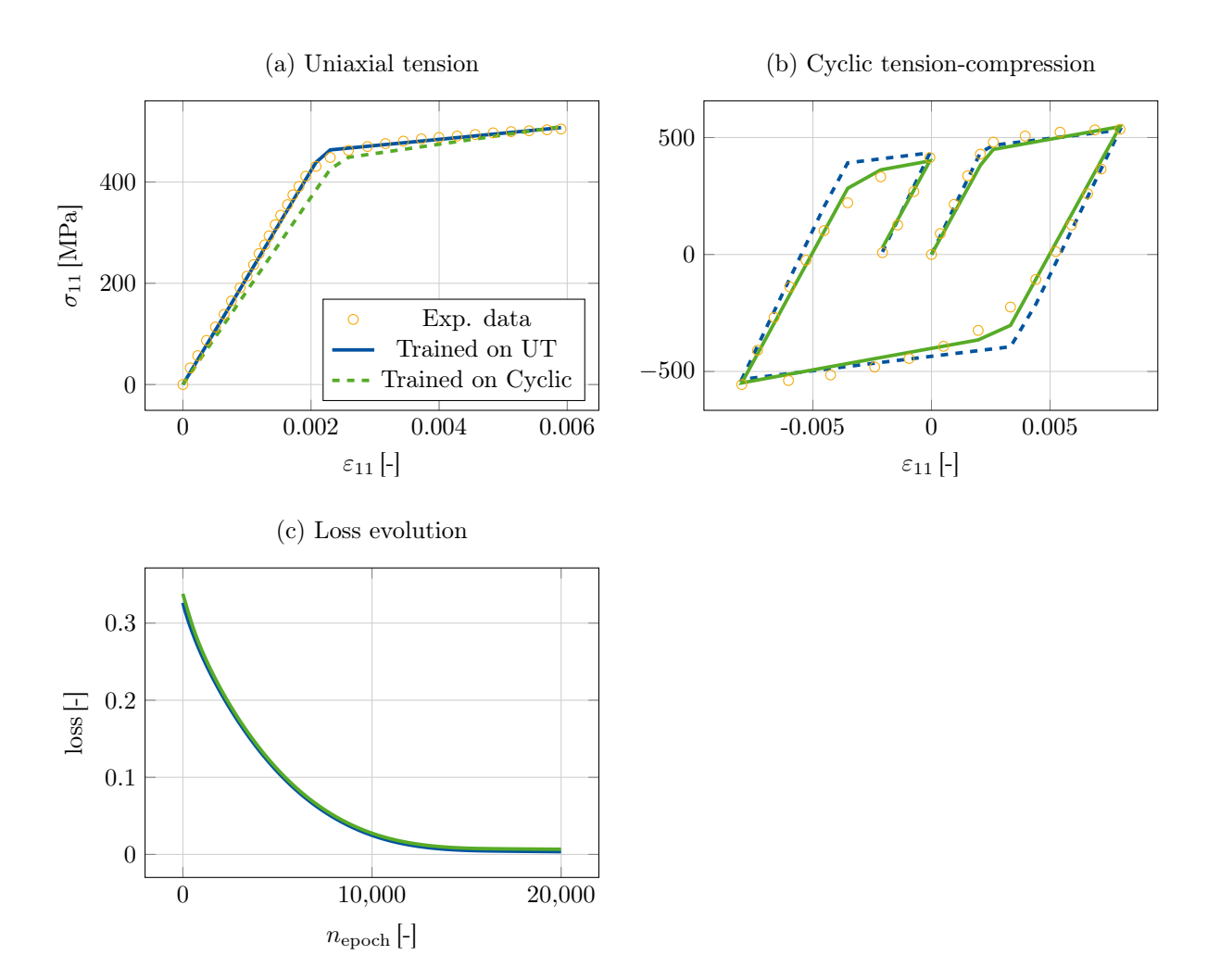


Figure 11: Training on experimental data from Kowalewski et al. (2014): Stress-strain curves for (a) uniaxial tension and (b) cyclic tension-compression tests. Comparison between experimental data (orange markers) and model predictions trained on uniaxial tension (blue, solid) and trained on cyclic loading (green, dashed). (c) Corresponding loss curves over the number of epochs.

The specification of inelasticity to plastic material behavior has not yet been captured. This work discussed the theory of plasticity and its formulation in terms of constitutive artificial neural networks. In addition to the approaches of general CANNs (Linka et al., 2021; Linka and Kuhl, 2023) and iCANNs (Holthusen et al., 2023a), a combination of a recurrent network with four feed-forward networks has been presented. The feed-forward networks described the elastic and plastic Helmholtz free energy, and inelastic potentials defining the yield surface and plastic flow to capture non-associative plasticity. Inclusion of plasticity required different numerical treatment compared to the previously mentioned works as it constrained the set of admissible stress states and return-mapping algorithms were necessary. This extension opens the application not only to plasticity but also to a broader range of material phenomena such as growth or reorientation as in (Soleimani et al., 2020; Holthusen et al., 2023b) or damage (see Holthusen et al. (2020, 2022); Felder et al. (2022)), for example. A co-rotated intermediate configuration has been used for the derivation and implementation of the model which is unaffected by the rotational non-uniqueness that goes along with the classical intermediate configuration that is generally used for the derivation of material models capturing inelasticity.

The performance of the presented network structure was investigated using synthetic and experimental data. Perfect plastic material behavior with a symmetric yield function and one including tension-compression asymmetry were investigated. The functions of the perfect plasticity model were exactly included in the formulation of the neural networks and the effect of different training sets on the model prediction has been evaluated. It was observed, that accurate predictions have already been observed for a training set on uniaxial tension only, but with an increase in training sets, such as uniaxial compression, equibiaxial tension and pure shear, the qualitative results converged to the exact solution. While the perfect plasticity model could perfectly be captured by the neural network structure, we examined its performance regarding tension-compression asymmetry as the current framework could not capture asymmetric yield functions. Again, several training sets of uni- and equibiaxial tension and compression have been investigated, and revealed that the chosen stress and error measure influenced the predicted results. This was caused by the second Piola-Kirchhoff stress chosen as the stress measure trained on, whose absolute value becomes greater in the compression range than in the tension range and, thus, is significant in the training process. This observation highlights that the error measure should be adjusted once asymmetric yield surfaces are captured by the model. In addition, synthetic data including kinematic hardening have been used to investigate the performance of the additional network of the Helmholtz free energy corresponding to kinematic hardening. Again, the predicted model met the experimental data qualitatively in the training and testing set while also the artificially generated yield surface and the predicted one are in alignment in the initial state and after the maximum tensile loading. Finally, experimental data of uniaxial and cyclic loads were used as inputs. Similarly, we observe good agreement between the experimental and predicted data, which underlines the application of the iCANNs including plasticity to predict realistic material behavior instead of fitting stressstrain data only.

Incorporation of plasticity theory into the class of iCANNs already shows promising results to predict material models of new materials that undergo irreversible deformations. However, this concept should be extended to a wider range of effects such as isotropic hardening or tension-compression asymmetry. In addition, plasticity theory should be combined with the approaches of visco-elasticity, growth, or damage mechanisms in order to end up with a flexible tool. We can then use machine learning as a promising tool to predict material models of new, innovative materials.

Appendix A. Appendix

Appendix A.1. Predicted weights of numerical results

Table A.4: Predicted weights of the elastic Helmholtz free energy for perfect plasticity for the corresponding training sets presented in the headline.

	UT	UT, UC	UT, EB	UT, UC, EB	UT, UC, EB, PS
$w_{1,1}^{\psi_e}$	0.2512	2.137e-2	8.611e-16	4.626e-33	1.128e-33
$w_{1,2}^{\psi_e}$	7.135e-10	3.731e-33	4.717e-33	3.817e-33	2.036e-33
$w_{1,3}^{\psi_e}$	0.9687	1.009	1.068	0	1.067
$w_{1,4}^{\psi_e}$	9.645e-3	1.294e-33	3.024e-33	0	2.448e-33
$w_{2,1}^{\psi_e}$	0.4689	0.5345	0.4298	0.799	0.4242
$w_{2,2}^{\psi_e}$	0.1148	1.265e-2	4.843e-16	7.784e-33	0
$w_{2,3}^{\psi_e}$	5.640e-3	8.763e-4	4.883e-3	6.148e-3	2.040e-3
$w_{2,4}^{\psi_e}$	5.816e-12	0	0	0	5.508e-33
$w_{2,5}^{\psi_e}$	1.244	1.078	1.060	2.007	1.017
$w_{2,6}^{\psi_e}$	1.032	1.020	1.064	0	$1.065\mathrm{e}{+0}$
$w_{2,7}^{\psi_e}$	0.2572	0	2.691e-2	3.794e-2	9.848e-3
$w_{2,8}^{\psi_e}$	3.867e-4	0	6.025e-33	0	2.491e-33
$w_{3,1}^{\psi_e}$	1.506e-12	7.810e-34	-2.595e-33	7.255e-34	2.837e-33
$w_{3,2}^{\psi_e}$	3.830e-22	3.856e-33	-3.492e-33	-4.404e-33	3.245e-33

Table A.5: Predicted weights of the elastic Helmholtz free energy for perfect plasticity with tension-compression asymmetry for the corresponding training sets presented in the headline.

	UT	UT, EB	UT, UC
$w_{1,1}^{\psi_e}$	2.388e-1	1.488e-1	0
$w_{1,2}^{\psi_e}$	9.160e-19	0	0
$w_{1,3}^{\psi_e}$	9.009e-1	9.294e-1	3.377e-1
$w_{1,4}^{\psi_e}$	0	0	0
$w_{2,1}^{\psi_e}$	9.922e-1	7.519e-1	1.304 e+0
$w_{2,2}^{\psi_e}$	1.191e-1	1.452e-1	$1.964 e{+0}$
$w_{2,3}^{\psi_e}$	5.827e-3	1.631e-2	0
$w_{2,4}^{\psi_e}$	6.238e-18	0	1.273e-4
$w_{2,5}^{\psi_e}$	1.123e+0	$1.091\mathrm{e}{+0}$	6.155e-1
$w_{2,6}^{\psi_e}$	1.038e+0	$1.060 \mathrm{e}{+0}$	1.783e+0
$w_{2,7}^{\psi_e}$	4.833e-2	8.707e-2	0
$w_{2,8}^{\psi_e}$	0	4.476e-33	3.309e-1
$w_{3,1}^{\psi_e}$	2.184e-5	-1.875e+0	-5.360e-33
$w_{3,2}^{\psi_e}$	1.260e-12	$1.303\mathrm{e}{+0}$	3.703e-33

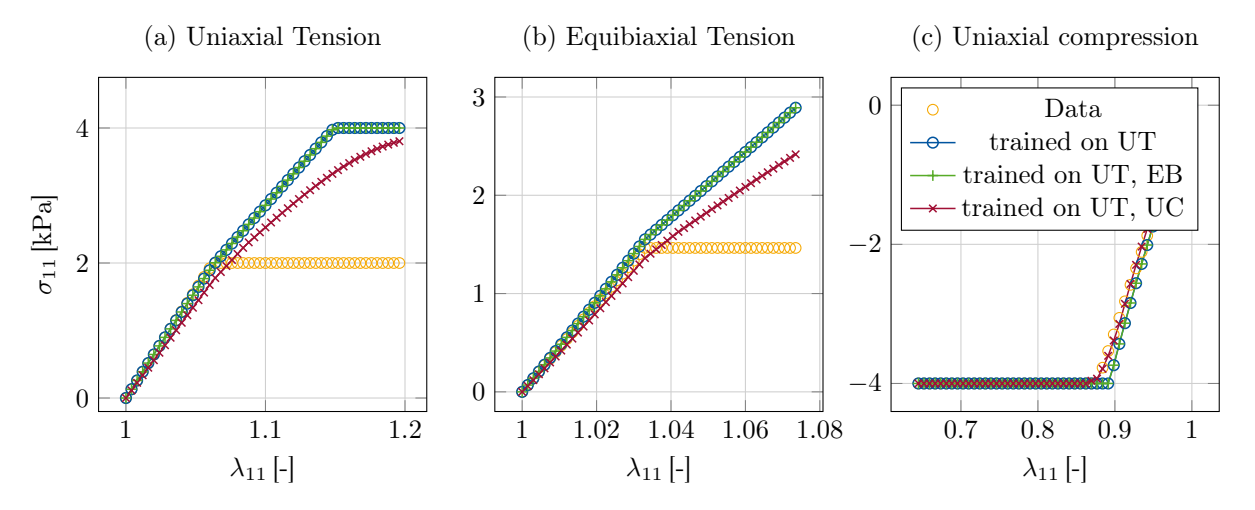


Figure A.12: Training on artificially generated data with the Tschoegel yield criterion (c.f. Equation (29)): Stress-strain curves of (a) uniaxial tension, (b) equibiaxial tension, (c) uniaxial compression.

Table A.6: Pre-training on experimental data: Predicted weights of the elastic and plastic Helmholtz free energies and the plastic potential included in the yield function for the training on uniaxial tension.

	Pre-training on UT						
$\phantom{aaaaaaaaaaaaaaaaaaaaaaaaaaaaaaaaaaa$	ψ_e	ψ_p	g				
$w_{1,1}^{\psi_e}$	2.185321	0.15263663	0.34382284				
$w_{1,2}^{\psi_e}$	9.596538	0.8169661	0.71375465				
$w_{1,3}^{\psi_e}$	13.198158	-	0.9144478				
$w_{1,4}^{\psi_e}$	5.693951	-	-				
$w_{2,1}^{\psi_e}$	2.185321	0.13491707	1.4719921e-01				
$w_{2,2}^{\psi_e}$	1.8050966	0.00127278	4.1532476e-26				
$w_{2,3}^{\psi_e}$	9.596538	0.04578267	1.0537818e-01				
$w_{2,4}^{\psi_e}$	0	0.1035376	$1.5691694 \mathrm{e}\hbox{-}02$				
$w_{2,5}^{\psi_e}$	13.198158	-	$1.0319424\mathrm{e}{+00}$				
$w_{2,6}^{\psi_e}$	1.6541797	-	$4.5209969 \mathrm{e}\hbox{-}03$				
$w_{2,7}^{\psi_e}$	5.693951	-	-				
$w_{2,8}^{\psi_e}$	0	-	-				
$w_{3,1}^{\psi_e}$	1.0693272	1.0693272	-				
$w_{3,2}^{\psi_e}$	0.02013625	0.02013625	-				

Table A.7: Training on experimental data: Predicted weights of the elastic and plastic Helmholtz free energies and the plastic potential included in the yield function for the training on uniaxial tension and on cyclic loading.

Trained on:	UT				Cyclic loadin	g
i	ψ_e	ψ_p	g	ψ_e	ψ_p	g
$w_{1,1}^{i}$	$5.693e{+1}$	$1.540\mathrm{e}{+1}$	3.438e-1	$5.776\mathrm{e}{+1}$	$1.358\mathrm{e}{+1}$	3.438e-1
$w_{1,2}^i$	$3.604 e{+1}$	$1.928\mathrm{e}{+1}$	7.138e-1	$3.604e{+1}$	$1.556\mathrm{e}{+1}$	7.138e-1
$w_{1,3}^i$	$2.018e{+1}$	-	1.495 + 1	2.137e + 1	-	$1.424 e{+1}$
$w_{1,4}^i$	0	-	-	0	-	-
$w_{2,1}^{i}$	2.339e-2	3.089e-3	0	1.913e-2	7.284e-3	6.052e-6
$w_{2,2}^i$	1.333e+0	4.833e-2	0	1.107e + 0	9.941e-2	0
$w_{2,3}^i$	6.864e-8	8.137e-3	0	6.733e-7	1.932e-2	0
$w_{2,4}^i$	1.746e-6	0.1573	0	2.919e-5	3.002e-1	0
$w_{2,5}^i$	6.126e-2	-	5.898e-3	4.991e-2	-	7.092e-3
$w_{2,6}^i$	1.227e+0	-	8.300 e-2	$1.060 \mathrm{e}{+0}$	-	9.440e-2
$w_{2,7}^i$	4.651e-7	-	-	4.598e-6	-	-
$w_{2,8}^i$	0	-	-	0	-	
$w_{3,1}^i$	1.069e + 0	1.069e + 0	-	1.071e + 0	$1.071\mathrm{e}{+0}$	-
$w_{3,2}^i$	0	0	-	0	0	-

Appendix B. Declarations

Data availability

Our source code and examples are available under 10.5281/zenodo.12706647 latest after publication.

CRediT authorship contribution statement

Birte Boes: Conceptualization, Methodology, Software, Formal analysis, Data Curation, Investigation, Validation, Writing – Original Draft, Writing – Review & Editing. **Jaan-Willem Simon**: Funding acquisition, Writing – Review & Editing. **Hagen Holthusen**: Conceptualization, Methodology, Software, Formal analysis, Writing – Review & Editing.

Acknowledgements

The authors gratefully acknowledge the financial support of the project SI 1959/12-1 (project number: 466117814) and TRR 280 (project number: 417002380) by the German Research Foundation (Deutsche Forschungsgemeinschaft, DFG).

Furthermore, the authors would like to express their gratitude to the help and experience of Jannick Kehls concerning numerical aspects.

References

References

- Abadi, M., Agarwal, A., Barham, P., Brevdo, E., Chen, Z., Citro, C., Corrado, G. S., Davis, A., Dean, J., Devin, M., et al., 2016. Tensorflow: Large-scale machine learning on heterogeneous distributed systems. arXiv preprint arXiv:1603.04467.
- Abdolazizi, K. P., Linka, K., Cyron, C. J., 2023. Viscoelastic constitutive artificial neural networks (vcanns)—a framework for data-driven anisotropic nonlinear finite viscoelasticity. arXiv preprint arXiv:2303.12164.
- Adhikary, D. P., Jayasundara, C. T., Podgorney, R. K., Wilkins, A. H., 2017. A robust return-map algorithm for general multisurface plasticity. International Journal for Numerical Methods in Engineering 109 (2), 218–234.
- Alzweighi, M., Tryding, J., Mansour, R., Borgqvist, E., Kulachenko, A., 2023. Anisotropic damage behavior in fiber-based materials: Modeling and experimental validation. Journal of the Mechanics and Physics of Solids 181, 105430.
- Amos, B., Xu, L., Kolter, J. Z., 2017. Input convex neural networks. In: Precup, D., Teh, Y. W. (Eds.), Proceedings of the 34th International Conference on Machine Learning. Vol. 70 of Proceedings of Machine Learning Research. PMLR, pp. 146–155.
- Aoyagi, Y., Tsuru, T., Shimokawa, T., 2014. Crystal plasticity modeling and simulation considering the behavior of the dislocation source of ultrafine-grained metal. International Journal of Plasticity 55, 43–57.
- Bedzra, R., Li, Y., Reese, S., Simon, J.-W., 2019. A comparative study of a multi-surface and a non-quadratic plasticity model with application to the in-plane anisotropic elastoplastic modelling of paper and paperboard. Journal of Composite Materials 53 (6), 753–767.
- Bedzra, R., Reese, S., Simon, J.-W., 2017. Meso-macro modelling of anisotropic metallic composites within the framework of multisurface plasticity. International Journal of Solids and Structures 120, 186–198.

- Blatz, P., Ko, W., 1962. Application of finite elastic theory to the deformation of rubbery materials. Transactions of the Society of Rheology 6, 223–251.
- Boes, B., Simon, J.-W., Reese, S., Holthusen, H., 2023. A novel continuum mechanical framework for decoupled material behavior in thickness and in-plane directions. Computer Methods in Applied Mechanics and Engineering 415, 116192.
- Borja, R. I., 2013. Plasticity. Springer Berlin Heidelberg. doi 10, 978-3.
- Chen, W.-F., 2007. Plasticity in reinforced concrete. J. Ross Publishing.
- Chun, B., Jinn, J., Lee, J., 2002. Modeling the bauschinger effect for sheet metals, part i: theory. International Journal of Plasticity 18 (5-6), 571–595.
- Coleman, B. D., Noll, W., 1961. Foundations of linear viscoelasticity. Reviews of modern physics 33 (2), 239.
- Coulomb, C. A., 1776. Essai sur une application des regles des maximis et minimis à quelques problèmes de statique relatifs à l'architecture. Mémoires de l'Académie Royale des Sciences 7, 343–387.
- de Souza Neto, E. A., Peric, D., Owen, D. R., 2011. Computational methods for plasticity: theory and applications. John Wiley & Sons.
- Desai, C. S., Siriwardane, H. J., 1984. Constitutive laws for engineering materials, with emphasis on geologic materials. (No Title).
- Drew, P. J., Monson, J. R., 2000. Artificial neural networks. Surgical Oncology Clinics of North America 9 (4), 767–781.
- Felder, S., Holthusen, H., Hesseler, S., Pohlkemper, F., Gries, T., Simon, J.-W., Reese, S., 2020. Incorporating crystallinity distributions into a thermo-mechanically coupled constitutive model for semi-crystalline polymers. International Journal of Plasticity 135, 102751.
- Felder, S., Kopic-Osmanovic, N., Holthusen, H., Brepols, T., Reese, S., 2022. Thermo-mechanically coupled gradient-extended damage-plasticity modeling of metallic materials at finite strains. International Journal of Plasticity 148, 103142.
- Flory, P., 1961. Thermodynamic relations for high elastic materials. Transactions of the Faraday Society 57, 829–838.
- Fuhg, J. N., Hamel, C. M., Johnson, K., Jones, R., Bouklas, N., 2023. Modular machine learning-based elastoplasticity: generalization in the context of limited data. Computer Methods in Applied Mechanics and Engineering 407, 115930.
- Gau, J.-T., Kinzel, G. L., 2001. An experimental investigation of the influence of the bauschinger effect on springback predictions. Journal of Materials Processing Technology 108 (3), 369–375.
- Gesto Beiroa, J. M., Gens Solé, A., Vaunat, J., 2011. Smoothing of yield surfaces and a reformulation of multi-surface plasticity. In: COMPLAS XI: proceedings of the XI International Conference on Computational Plasticity: fundamentals and applications. CIMNE, pp. 921–931.
- Ghaboussi, J., Garrett, J. H., Wu, X., 1991. Knowledge-based modeling of material behavior with neural networks. Journal of Engineering Mechanics 117, 132–153.
- Ghaderi, A., Morovati, V., Dargazany, R., 2020. A physics-informed assembly for feed-forward neural network engines to predict inelasticity in cross-linked polymers. Polymers 12, 2628.
- Ghorbanpour, S., Alam, M. E., Ferreri, N. C., Kumar, A., McWilliams, B. A., Vogel, S. C., Bicknell, J., Beyerlein, I. J., Knezevic, M., 2021. Experimental characterization and crystal plasticity modeling of anisotropy, tension-compression asymmetry, and texture evolution of additively manufactured inconel 718 at room and elevated temperatures. International Journal of Plasticity 135, 102786.
- Ghorbel, E., 2008. A viscoplastic constitutive model for polymeric materials. International Journal of Plasticity 24 (11), 2032–2058.
- Gurtin, M. E., 1982. An introduction to continuum mechanics. Academic press.
- Haghighat, E., Abouali, S., Vaziri, R., 2023. Constitutive model characterization and discovery using physics-informed deep learning. Engineering Applications of Artificial Intelligence 120, 105828.
- Hartmann, S., Neff, P., 2003. Polyconvexity of generalized polynomial-type hyperelastic strain energy functions for near-

- incompressibility. International journal of solids and structures 40 (11), 2767–2791.
- He, X., Chen, J., 2022. Thermodynamically consistent machine-learned internal state variable approach for data-driven modeling of path-dependent materials. Computer Methods in Applied Mechanics and Engineering 402, 115348.
- Hencky, H., 1924. Zur theorie plastischer zustände. Zeitschrift für angewandte Mathematik und Mechanik 4 (4), 323-334.
- Hill, R., 1952. The mathematical theory of plasticity. Bull. Am. Math. Soc 58, 507-512.
- Holthusen, H., Brepols, T., Reese, S., Simon, J.-W., 2020. An anisotropic constitutive model for fiber-reinforced materials including gradient-extended damage and plasticity at finite strains. Theoretical and Applied Fracture Mechanics 108, 102642.
- Holthusen, H., Brepols, T., Reese, S., Simon, J.-W., 2022. A two-surface gradient-extended anisotropic damage model using a second order damage tensor coupled to additive plasticity in the logarithmic strain space. Journal of the Mechanics and Physics of Solids 163, 104833.
- Holthusen, H., Lamm, L., Brepols, T., Reese, S., Kuhl, E., 2023a. Theory and implementation of inelastic constitutive artificial neural networks. arXiv preprint arXiv:2311.06380.
- Holthusen, H., Rothkranz, C., Lamm, L., Brepols, T., Reese, S., 2023b. Inelastic material formulations based on a co-rotated intermediate configuration application to bioengineered tissues. Journal of the Mechanics and Physics of Solids 172, 105174.
- Holzapfel, G. A., 2002. Nonlinear solid mechanics: a continuum approach for engineering science. Meccanica 37 (4), 489-490.
- Hou, J., Chen, X., Wu, T., Kuhl, E., Wang, X., 2024. Automated data-driven discovery of material models based on symbolic regression: A case study on human brain cortex. arXiv preprint arXiv:2402.05238.
- Houlsby, G. T., Puzrin, A. M., 2007. Advanced Plasticity Theories. Springer.
- Kalina, K. A., Gebhart, P., Brummund, J., Linden, L., Sun, W., Kästner, M., 2023a. Neural network-based multiscale modeling of finite strain magneto-elasticity with relaxed convexity criteria. Computer Methods in Applied Mechanics and Engineering.
- Kalina, K. A., Linden, L., Brummund, J., Kästner, M., 2023b. Fe ann: an efficient data-driven multiscale approach based on physics-constrained neural networks and automated data mining. Computational Mechanics 71 (5), 827–851.
- Kalina, K. A., Linden, L., Brummund, J., Metsch, P., Kästner, M., 2022. Automated constitutive modeling of isotropic hyperelasticity based on artificial neural networks. Computational Mechanics 69, 213–232.
- Karniadakis, G. E., Kevrekidis, I. G., Lu, L., Perdikaris, P., Wang, S., Yang, L., 2021. Physics-informed machine learning. Nature Reviews Physics 3, 422–440.
- Keralavarma, S. M., 2017. A multi-surface plasticity model for ductile fracture simulations. Journal of the Mechanics and Physics of Solids 103, 100–120.
- Kowalewski, Z. L., Szymczak, T., Maciejewski, J., 2014. Material effects during monotonic-cyclic loading. International Journal of Solids and Structures 51 (3-4), 740–753.
- $Kuhlmann-Wilsdorf,\ D.,\ 1999.\ The\ theory\ of\ dislocation-based\ crystal\ plasticity.\ Philosophical\ Magazine\ A\ 79\ (4),\ 955-1008.$
- Lamm, L., Holthusen, H., 2022. A macroscopic approach for stress-driven anisotropic growth in bioengineered soft tissues. Biomechanics and Modeling in Mechanobiology 21 (2), 627–645.
- Lamm, L., Holthusen, H., Böhm, C., Jockenhövel, S., Reese, S., 2021. Macroscopic modelling of stress driven anisotropic growth in bioengineered tissues. PAMM 21 (1), e202100046.
- Lee, E., Liu, D., 1967. Finite-strain elastic-plastic theory with application to plane-wave analysis. Journal of applied physics 38 (1), 19–27.
- Lee, E. H., 1969. Elastic-plastic deformation at finite strains. Journal of Applied Mechanics 36 (1), 1–6.
- Linden, L., Klein, D. K., Kalina, K. A., Brummund, J., Weeger, O., Kästner, M., 2023. Neural networks meet hyperelasticity: A guide to enforcing physics. Journal of the Mechanics and Physics of Solids.
- Linka, K., Hillgartner, M., Abdolazizi, K. P., Aydin, R. C., Itskov, M., Cyron, C. J., 2021. Constitutive artificial neural networks: A fast and general approach to predictive data-driven constitutive modeling by deep learning. Journal of Computational Physics 429, 110010.

- Linka, K., Kuhl, E., 2023. A new family of constitutive artificial neural networks towards automated model discovery. Computer Methods in Applied Mechanics and Engineering 403, 115731.
- Linka, K., Schafer, A., Meng, X., Zou, Z., Karniadakis, G. E., Kuhl, E., 2022. Bayesian physics-informed neural networks for real-world nonlinear dynamical systems. Computer Methods in Applied Mechanics and Engineering. URL http://dx.doi.org/10.1016/j.cma.2022.115346
- Lubliner, J., 1985. A model of rubber viscoelasticity. Mechanics Research Communications 12 (2), 93-99.
- Malik, A., Abendroth, M., Hütter, G., Kiefer, B., 2021. A hybrid approach employing neural networks to simulate the elastoplastic deformation behavior of 3d-foam structures. Advanced Engineering Materials 24, 2100641.
- Martonová, D., Peirlinck, M., Linka, K., Holzapfel, G. A., Leyendecker, S., Kuhl, E., 2024. Automated model discovery for human cardiac tissue: Discovering the best model and parameters. Computer Methods in Applied Mechanics and Engineering 428, 117078.
- Masi, F., Stefanou, I., 2022. Multiscale modeling of inelastic materials with thermodynamics-based artificial neural networks (tann). Computer Methods in Applied Mechanics and Engineering 398, 115190.
- Masi, F., Stefanou, I., Vannucci, P., Maffi-Berthier, V., 2021. Thermodynamics-based artificial neural networks for constitutive modeling. Journal of the Mechanics and Physics of Solids 147, 104277.
- McCulloch, J. A., St. Pierre, S. R., Linka, K., Kuhl, E., 2024. On sparse regression, lp-regularization, and automated model discovery. International Journal for Numerical Methods in Engineering, e7481.
- Meyer, K. A., Ekre, F., 2023. Thermodynamically consistent neural network plasticity modeling and discovery of evolution laws. engrXiv.
- Miehe, C., 2002. Strain-driven homogenization of inelastic microstructures and composites based on an incremental variational formulation. International Journal for Numerical Methods in Engineering 55 (11), 1285–1322.
- Mollica, F., Srinivasa, A., 2002. A general framework for generating convex yield surfaces for anisotropic metals. Acta mechanica 154, 61–84.
- Motaman, S. A. H., Haase, C., 2021. The microstructural effects on the mechanical response of polycrystals: A comparative experimental-numerical study on conventionally and additively manufactured metallic materials. International Journal of Plasticity 135, 102941, available online 26 July 2021.
- Ogden, R. W., 1972. Large deformation isotropic elasticity—on the correlation of theory and experiment for incompressible rubberlike solids. Proceedings of the Royal Society of London. A. Mathematical and Physical Sciences 326 (1567), 565–584.
- Peirlinck, M., Linka, K., Hurtado, J. A., Kuhl, E., 2024. On automated model discovery and a universal material subroutine for hyperelastic materials. Computer Methods in Applied Mechanics and Engineering 418, 116534.

Ogden, R. W., 1997. Non-linear elastic deformations. Courier Corporation.

- Peng, G. C. Y., Alber, M., Buganza Tepole, A., et al., 2021. Multiscale modeling meets machine learning: What can we learn? Archives of Computational Methods in Engineering 28, 1017–1037.
- Pierre, S. R. S., Rajasekharan, D., Darwin, E. C., Linka, K., Levenston, M. E., Kuhl, E., 2023. Discovering the mechanics of artificial and real meat. Computer Methods in Applied Mechanics and Engineering 415, 116236.
- Raissi, M., Perdikaris, P., Karniadakis, G. E., 2019. Physics-informed neural networks: A deep learning framework for solving forward and inverse problems involving nonlinear partial differential equations. Journal of Computational Physics 378, 686–707
- Reuvers, M., Kulkarni, S., Boes, B., et al., 2024. A thermo-mechanically coupled constitutive model for semi-crystalline polymers at finite strains: Mechanical and thermal characterization of polyamide 6 blends. Continuum Mechanics and Thermodynamics 36, 657–698.
- Rosenkranz, M., Kalina, K. A., Brummund, J., Kästner, M., 2023a. A comparative study on different neural network architectures to model inelasticity. International Journal for Numerical Methods in Engineering, 1–39.

- Rosenkranz, M., Kalina, K. A., Brummund, J., Sun, W., Kästner, M., 2023b. Viscoelasticity with physics-augmented neural networks: Model formulation and training methods without prescribed internal variables.
 - URL https://doi.org/10.1016/j.cma.2023.116739
- Schröder, J., Neff, P., 2003. Invariant formulation of hyperelastic transverse isotropy based on polyconvex free energy functions. International journal of solids and structures 40 (2), 401–445.
- Settgast, C., Hütter, G., Kuna, M., Abendroth, M., 2020. A hybrid approach to simulate the homogenized irreversible elastic-plastic deformations and damage of foams by neural networks. International Journal of Plasticity 126, 102624.
- Shen, Y., Chandrashekhara, K., Breig, W., Oliver, L., 2004. Neural network based constitutive model for rubber material. Rubber Chemistry and Technology 77, 257–277.
- Simo, J., Taylor, R. L., Pister, K., 1985. Variational and projection methods for the volume constraint in finite deformation elasto-plasticity. Computer methods in applied mechanics and engineering 51 (1-3), 177–208.
- Simo, J. C., Hughes, T. J., 2006. Computational inelasticity. Vol. 7. Springer Science & Business Media.
- Simo, J. C., Taylor, R. L., 1991. Quasi-incompressible finite elasticity in principal stretches. continuum basis and numerical algorithms. Computer methods in applied mechanics and engineering 85 (3), 273–310.
- Soleimani, M., Muthyala, N., Marino, M., Wriggers, P., 2020. A novel stress-induced anisotropic growth model driven by nutrient diffusion: theory, fem implementation and applications in bio-mechanical problems. Journal of the Mechanics and Physics of Solids 144, 104097.
- Stier, B., Simon, J.-W., Reese, S., 2015. Comparing experimental results to a numerical meso-scale approach for woven fiber reinforced plastics. Composite structures 122, 553–560.
- Stockman, C. A., Goriely, A., Kuhl, E., 2024. Two for tau: Automated model discovery reveals two-stage tau aggregation dynamics in alzheimer's disease. bioRxiv, 2024–07.
- Svendsen, B., 2001. On the modelling of anisotropic elastic and inelastic material behaviour at large deformation. International Journal of Solids and Structures 38 (52), 9579–9599.
- Taç, V., Rausch, M. K., Costabal, F. S., Tepole, A. B., 2023. Data-driven anisotropic finite viscoelasticity using neural ordinary differential equations. Computer Methods in Applied Mechanics and Engineering 411, 116046.
- Terzaghi, K., Peck, R. B., Mesri, G., 1996. Soil mechanics in engineering practice. John wiley & sons.
- Tresca, H. E., 1869. Mémoire sur l'écoulement des corps solides. Imprimerie impériale.
- Truesdell, C., Noll, W., et al., 1992. The non-linear field theories of mechanics [electronic resource]. Encyclopedia of Physics.
- Tschoegl, N., 1971. Failure surfaces in principal stress space 32 (1), 239–267.
- Vlassis, N., Sun, W., 2021a. Component-based machine learning paradigm for discovering rate-dependent and pressure-sensitive level-set plasticity models. Journal of Applied Mechanics 89, 1–13.
- Vlassis, N., Sun, W., 2021b. Sobolev training of thermodynamic-informed neural networks for interpretable elasto-plasticity models with level set hardening. Computer Methods in Applied Mechanics and Engineering 377, 113695.
- von Mises, R., 1913. Mechanik der festen körper im plastisch-deformablen zustand. Nachrichten von der Gesellschaft der Wissenschaften zu Göttingen, Mathematisch-Physikalische Klasse, 582–592.
- Weber, P., Wagner, W., Freitag, S., 2023. Physically enhanced training for modeling rate-independent plasticity with feedforward neural networks. Computational Mechanics.
- Xia, Q. S., Boyce, M. C., Parks, D. M., 2002. A constitutive model for the anisotropic elastic–plastic deformation of paper and paperboard. International journal of solids and structures 39 (15), 4053–4071.
- Yu, M.-h., 2002. Advances in strength theories for materials under complex stress state in the 20th century. Appl. Mech. Rev. 55 (3), 169–218.
- Zhang, Z., Zou, Z., Kuhl, E., Karniadakis, G. E., 2024. Discovering a reaction-diffusion model for alzheimer's disease by combining pinns with symbolic regression. Computer Methods in Applied Mechanics and Engineering 419, 116647.

Zienkiewicz, O., 1977. Some useful forms of isotropic yield surface for soil and rock mechanics. Finite Elements in Geomechanics edited by Gudehus, G., 179–190.

Zopf, C., Kaliske, M., 2017. Numerical characterisation of uncured elastomers by a neural network based approach. Computers and Structures 182, 504–525.